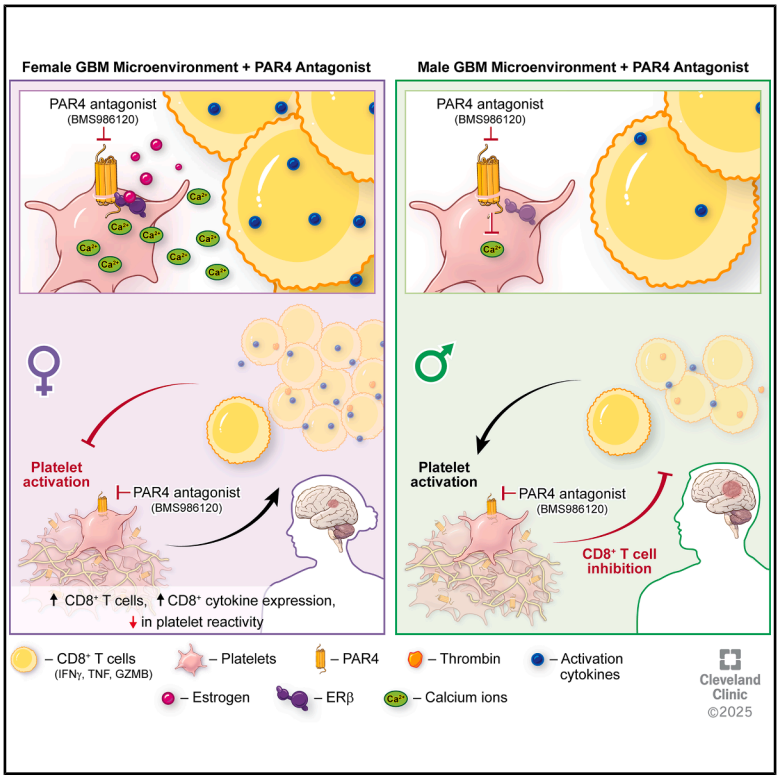
Cancer Cell

Article

A sex-specific platelet switch controls anti-tumor immunity in glioblastoma

Graphical abstract



Highlights

- PAR4 drives platelet hyperreactivity and immune suppression in GBM
- PAR4 inhibition prolongs survival exclusively in female GBM models
- Estrogen-ERβ signaling couples PAR4 blockade to CD8⁺ T cell activity
- Platelets and CD8⁺ T cells form a sex-specific immunoregulatory circuit

Authors

Anthony R. Sloan, George Bukenya, Gavin P. Tannish, ..., Andrew Dhawan, Scott J. Cameron, Justin D. Lathia

Correspondence

lathiaj@ccf.org

In brief

Sloan et al. show that platelets suppress anti-tumor immunity through PAR4 signaling in glioblastoma. Blocking PAR4 selectively benefits females by enhancing estrogen receptor β-dependent CD8⁺ T cell responses, uncovering a mechanism that links thrombosis, sex differences, and immunotherapy and suggesting new opportunities for precision cancer treatment.

Sloan et al., 2026, Cancer Cell *44*, 1–16
November 9, 2026 © 2026 The Author(s). Published by Elsevier Inc.
https://doi.org/10.1016/j.ccell.2026.10.004

CellPress

Please cite this article in press as: Sloan et al., A sex-specific platelet switch controls anti-tumor immunity in glioblastoma, Cancer Cell (2026), https://doi.org/10.1016/j.ccell.2026.10.004

Cancer Cell

CellPress
OPEN ACCESS

Article

A sex-specific platelet switch controls anti-tumor immunity in glioblastoma

Anthony R. Sloan,[1,2] George Bukenya,[1] Gavin P. Tannish,[1] Daniel J. Silver,[1,2,3] Anu Aggarwal,[4] Juyeun Lee,[1,2] Daniel Rosoff,[5,6] Tyler J. Alban,[1,2,3] Ivan Juric,[1,5] Shikha Parsai,[1,5] Vargab Baruah,[7] Tyler Bodovetz,[1,22] Donovan Whitfield,[1] Liza Tack,[1] Tanvi Navadgi,[1] Natalie Reitz,[1] Shawn T. Ho,[2,9] Aarav Badani,[1] Jessica Goldberg,[1] Xueer Yuan,[1] Aymerick Gaboriau,[1] Samrutha Kamatala,[1] Jesse Coker,[2,3] Vrishabhadev Sathish Kumar,[2,9] Saachi S. Jain,[2,9] Chang Xu,[1] Alliefair Scalise,[4,10,11] Bhairavi Rajasekar,[4,10,11] Alex Vincenti,[1] Erin E. Mulkearns-Hubert,[1,2,3] Craig M. Horbinski,[12] Andrew E. Sloan,[13] Christopher G. Hubert,[2,14] Jingqin Luo,[15] Joshua B. Rubin,[16,17] Evi X. Stavrou,[2,18,19] Falk W. Lohoff,[5,6] Wendy A. Goodman,[2,9] Tyler E. Miller,[2,9] Christine M. O'Connor,[2,3,7,8] Marvin T. Nieman,[2,20] Naseer Sangwan,[7] Timothy A. Chan,[1,2,3,21,22] Alok A. Khorana,[2,3,4,21] Andrew Dhawan,[1,2,3,22] Scott J. Cameron,[3,4,10,11] and Justin D. Lathia[1,2,3,22,23,*]

[1]Department of Cancer Sciences, Cleveland Clinic Research, Cleveland Clinic, Cleveland, OH 44195, USA
[2]Case Comprehensive Cancer Center, Cleveland, OH 44106, USA
[3]Cleveland Clinic Lerner College of Medicine of Case Western Reserve University, Cleveland, OH 44106, USA
[4]Department of Heart, Blood, and Kidney Research, Cleveland Clinic Research, Cleveland Clinic, Cleveland, OH 44195, USA
[5]Section on Clinical Genomics and Experimental Therapeutics, National Institute on Alcohol Abuse and Alcoholism, National Institutes of Health, Bethesda, MD 20892, USA
[6]NIH Oxford-Cambridge Scholars Program, National Institutes of Health, Bethesda, MD 20892, USA
[7]Microbial Sciences in Health, Cleveland Clinic Research, Cleveland Clinic, Cleveland, OH 44195, USA
[8]Sheika Fatima Bint Mubarak Global Center for Pathogen and Human Health Research, Cleveland Clinic Research, Cleveland Clinic, Cleveland, OH 44195, USA
[9]Department of Pathology, Case Western Reserve University School of Medicine, Cleveland, OH 44106, USA
[10]Department of Cardiovascular Medicine, Section of Vascular Medicine, Cleveland Clinic, Cleveland, OH 44195, USA
[11]Heart Vascular and Thoracic Institute, Department of Cardiovascular Medicine, Section of Vascular Medicine, Cleveland Clinic, Cleveland, OH 44195, USA
[12]Department of Laboratory Medicine and Pathology, Mayo Clinic Florida, Jacksonville, FL 32224, USA
[13]Neuroscience Institute and Department of Neurosurgery, Wright State University School of Medicine, Dayton, OH 45435, USA
[14]Department of Biochemistry, Case Western Reserve University School of Medicine, Cleveland, OH 44106, USA
[15]Department of Surgery, Washington University School of Medicine, St. Louis, MO 63110, USA
[16]Department of Pediatrics, Washington University School of Medicine, St. Louis, MO 63110, USA
[17]Department of Neurosciences, Washington University School of Medicine, St. Louis, MO 63110, USA
[18]Medicine Service, Section of Hematology-Oncology, Louis Stokes Veterans, Cleveland, OH, USA
[19]Department of Medicine, Hematology and Oncology Division, Case Western Reserve University School of Medicine, Cleveland, OH 44106, USA
[20]Department of Pharmacology, Case Western Reserve University School of Medicine, Cleveland, OH 44106, USA
[21]Taussig Cancer Institute, Cleveland Clinic, Cleveland, OH, USA
[22]Rose Ella Burkhardt Brain Tumor & Neuro-Oncology Center, Cleveland Clinic, Cleveland, OH, USA
[23]Lead contact
*Correspondence: lathiaj@ccf.org
https://doi.org/10.1016/j.ccell.2026.10.004

SUMMARY

Sex differences in glioblastoma (GBM) outcomes are shaped by biological, hormonal, and immune factors, but the mechanisms driving these disparities remain unclear. We identify platelet protease-activated receptor 4 (PAR4) signaling as a regulator of sex-specific anti-tumor immunity. GBM patients exhibit increased platelet reactivity driven by PAR4. In murine models, pharmacologic or genetic inhibition of PAR4 prolongs survival in females, but not males, and is estrogen dependent, persisting in hormonal females regardless of chromosomal sex. The survival advantage is mediated within the tumor microenvironment through enhanced $CD8^+$ T cell infiltration and function. PAR4-activated platelets suppress $CD8^+$ T cell activity, whereas $CD8^+$ T cell depletion abolishes both tumor-induced platelet reactivity and the PAR4-dependent survival advantage. Mechanistically, PAR4 inhibition enhances $CD8^+$ T cell signaling through interaction with estrogen receptor β (ERβ). These findings demonstrate that platelets are critical regulators of sex-specific anti-tumor immunity and identify PAR4 as a promising therapeutic target in cancer.

This is an open access article under the CC BY-NC-ND license (http://creativecommons.org/licenses/by-nc-nd/4.0/).

Please cite this article in press as: Sloan et al., A sex-specific platelet switch controls anti-tumor immunity in glioblastoma, Cancer Cell (2026), https://doi.org/10.1016/j.ccell.2026.10.004

INTRODUCTION

Sex differences underlie and influence risk, progression, and treatment outcomes across many cancers. For example, men are more likely to develop several cancer types, including glioblastoma (GBM), while women often exhibit better survival rates.[1,2] Despite these appreciated epidemiological differences, treatment paradigms remain uniform, highlighting the opportunity for sex-specific therapies shaped by hormonal, genetic, and immune differences. Sex differences in cancer also involve the tumor microenvironment (TME), a complex network of cells and anatomical structures, including resident neural populations, blood vessels, and infiltrating immune cells, that interact with tumors. Among components of the TME, platelets play a major role in maintaining vascular integrity and modulating immune responses, potentially contributing to sex differences in cancer progression. While platelets are present in the TME and known to influence immune cells, their role in cancer, particularly in thrombotic events and sex differences via thrombin-PAR4 signaling, remains underexplored.[3–6] In a recent study, the antiplatelet drug aspirin, which inhibits cyclooxygenase-1 and cyclooxygenase-2, enhanced the protective mechanism of T cells and, therefore, inhibited metastasis in murine models of lung and liver malignancies, supporting a role for platelets in cancer progression.[7]

In GBM, the most common primary malignant brain tumor in adults, immune cells in the TME suppress anti-tumor responses. Myeloid-derived suppressor cells (MDSCs) drive immune suppression in GBM, while lymphocytes, such as $CD8^+$ T cells, are reduced and have decreased function.[8–10] Moreover, GBM has a striking sex difference in incidence and prognosis, with men 1.6 times more likely to develop the disease and exhibiting shorter survival.[2,11] Both intrinsic factors and immune cells such as microglia, MDSCs, and $CD8^+$ T cells contribute to these differences,[8,10,12] with myeloid-derived cells having enhanced proliferation in males and male $CD8^+$ T cells showing a greater propensity for exhaustion.[10] Although platelet-derived factors are known to promote tumor growth, their underlying mechanisms and role in sex-based differences in GBM are unclear.[4,13] Thrombotic events, such as deep vein thrombosis (DVT) and pulmonary embolism (PE), are common in cancer patients and a leading cause of morbidity and mortality, although the cause of death is not attributed to intravascular thrombosis.[14,15] GBM patients face a 15%–24% risk of thrombotic events, and patients with thrombotic events have worse outcomes, suggesting that a pro-thrombotic state drives cancer progression.[6,16–18] Therefore, given that the sex difference in GBM incidence and aggressiveness is partly attributable to a more immunosuppressive TME in males, we sought to determine whether sex-dependent platelet signaling contributes to this immunosuppressive microenvironment.

RESULTS

PAR4 signaling drives hyperactive platelets in GBM patients

The GBM TME shapes tumor growth and response to therapy through a variety of mechanisms[1]; however, the role of platelets within this microenvironment has not been fully elucidated. We and others have previously reported that high platelet counts are temporally related to worsened clinical outcomes in patients with any malignancy, including GBM.[4,19,20] By carefully evaluating a platelet transcriptomic signature in the context of large-scale human datasets, we found that an enrichment of a platelet gene signature is associated with poor overall survival in GBM patients (Figure 1A; Table S1)[21] and negatively correlated with several anti-tumor immune cell populations including T cells, dendritic cells (DCs), and B cells (Figure S1; Table S2). These data suggest that platelet-associated gene signatures correlate with poorer prognosis and an immunosuppressive landscape in GBM.

Next, we asked whether GBM patients have altered platelet physiology when compared to age- and sex-matched control subjects. We measured platelet reactivity from peripheral blood from GBM patients and control subjects using assays that measure degranulation of platelet contents (Tables S3 and S4). Platelets from both male and female GBM patients had increased agonist-induced reactivity, measured by P-selectin, due to protease-activated receptor 4 (PAR4) signaling (Figures 1B and S2A–S2C). However, agonist-induced platelet reactivity via protease-activated receptor 1 (PAR1), purinergic receptor P2Y12, and the thromboxane receptor (TXA2) was similar or not as drastically different between GBM and control subjects (Figures S2D–S2F). Thrombin is a potent human platelet agonist that acts via the PAR1 and PAR4 receptors and is quantified by measuring plasma levels of the thrombin-antithrombin (TAT) complex. We found that GBM patients had significantly higher TAT levels relative to healthy age-matched control subjects (Figure 1C). Consistently, *in vivo* studies utilizing murine GBM models demonstrated that tumor-bearing mice had increased circulating platelet factor 4 expression (Figure 1D) and increased platelet reactivity compared to their baseline pre-tumor state (Figures 1E and 1F), with no difference in spontaneous or thrombin-induced platelet reactivity between male and female mice (Figures S2G–S2J). Likewise, across patients with GBM, using Mendelian randomization analyses, we found that PAR4 expression was predictive of GBM diagnosis, whereas other platelet receptor expression was not predictive (Figures S3A–S3C). These findings are consistent with previous reports indicating that agonist-induced platelet activation and spontaneous platelet activation were both increased in patients with late-stage metastatic cancer[22] and further suggest that tumor-induced platelet reactivity is mediated by PAR4.

Inhibiting platelets via the thrombin-PAR4 signaling axis prolongs survival in a sex-dependent manner

To investigate the role of platelets in GBM tumor progression, we intracranially transplanted C57BL/6 mice with murine GBM cells followed by subsequent depletion of platelets through intravenous administration of anti-glycoprotein 1b (GP1b) antibody and survival analysis. These proof-of-concept studies demonstrated that platelet depletion prolongs survival in female tumor-bearing mice (Figures 2A and S4A). Depletion of platelets had no effect in male mice in either tumor model (Figures 2B and S4B), despite achieving comparable levels of platelet depletion in both sexes, approximately 90% in the SB28 model (Figure 2C) and 80% in the KR158 model (Figure S4C). These results, in combination with the positive correlation between

Please cite this article in press as: Sloan et al., A sex-specific platelet switch controls anti-tumor immunity in glioblastoma, Cancer Cell (2026), https://doi.org/10.1016/j.ccell.2026.10.004

CellPress
OPEN ACCESS

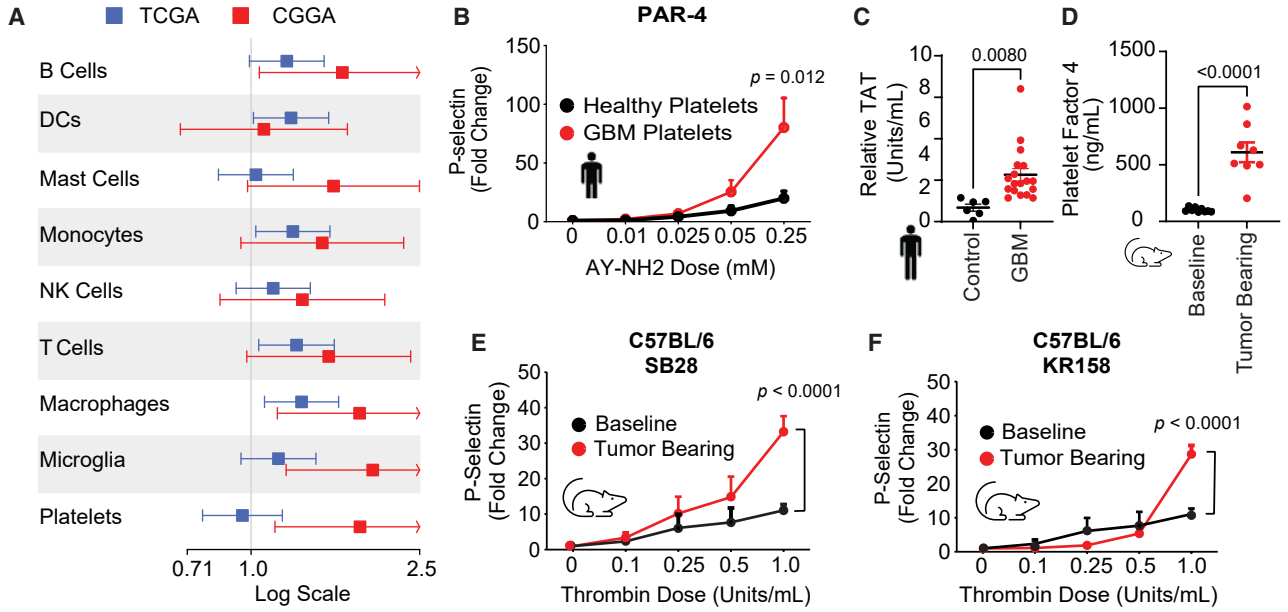


Figure 1. PAR4 signaling drives hyperactive platelets in GBM patients

(A) WHO grade 4 Isocitrate dehydrogenases (IDH)-wild-type GBM samples from The Cancer Genome Atlas ([TCGA], $n = 148$) and Chinese Glioma Genome Atlas ([CGGA_325], $n = 98$) datasets were analyzed. Univariate Cox proportional hazards models were constructed, and deconvoluted immune cell proportions and platelet signature scores were Z score normalized and centered prior to hazard ratio computation. Hazard ratios represent overall survival as a function of immune cell proportion or platelet signature score and are displayed with 95% confidence intervals.

(B) Washed platelets isolated from patients with glioblastoma (GBM) and age- and sex-matched control subjects were stimulated with AY-NH2 to activate protease-activated receptor 4 (PAR4). α-Granule secretion was measured by flow cytometry using a P-selectin-specific antibody. Data are presented as mean ± SEM from $n = 13$ GBM patients and $n = 18$ control subjects. Statistical significance was determined by two-way ANOVA.

(C) Plasma thrombin-antithrombin (TAT) complex levels in GBM patients and healthy control subjects were measured by ELISA. Data are presented as mean ± SEM from $n = 18$ GBM patients and $n = 6$ control subjects. Statistical significance was determined by unpaired Student's t test.

(D) Serum was collected from mice before intracranial tumor implantation (baseline) and following implantation of SB28 glioblastoma cells. Platelet factor 4 (PF4) levels were measured by ELISA. Data are presented as mean ± SEM from $n = 8$ baseline and $n = 8$ tumor-bearing mice. Statistical significance was determined by unpaired Student's t test.

(E and F) Washed platelets were isolated before intracranial tumor implantation (baseline) and following implantation of SB28 (E) or KR158 (F) GBM cells.Washed platelets were stimulated with thrombin and platelet α-granule secretion was measured by flow cytometry using a P-selectin-specific antibody. Data are presented as mean ± SEM from $n = 4$ independent experiments. Statistical significance was determined by two-way ANOVA. Note: the same baseline (non-tumor-bearing) animals are shown in both (E) and (F) for comparison.

platelet expression and intratumoral immunosuppressive immune cell populations (Figure 1A), suggest that platelets drive tumor growth in a sex-biased manner, prompting us to question whether inhibiting the enhanced PAR4-mediated platelet reactivity may also show a sex difference in survival benefit.

We next transplanted C57BL/6 mice with murine GBM cells and pharmacologically targeted the major platelet PAR receptor in mice (PAR4) with daily oral gavage treatment with the PAR4 antagonist BMS986120. Inhibiting PAR4 in tumor-bearing mice prolonged survival in a sex-dependent manner, with a marked survival increase in females and no impact in males in all three murine GBM models tested (Figures 2D–2G, S5A, and S5B). We further confirmed this sex-specific survival advantage using dabigatran, a direct inhibitor of thrombin, the PAR4 ligand (Figures S5C and S5D). To determine whether these effects were due to higher PAR4 expression in females, we examined intratumoral PAR4 (*F2RL3*) expression in GBM patient samples (The Cancer Genome Atlas [TCGA]) and found no difference in expression between tumors from males and those from females (Figure S5E). Subsequently, we measured surface and total PAR4 expression on mouse platelets and found no difference in expression between males and females (Figures S5F and S5G). Lastly, treatment with BMS986120 did not improve survival in PAR4$^{-/-}$ mice bearing intracranial SB28 tumors (Figure S5H), indicating that the survival benefit observed with pharmacologic PAR4 inhibition is abolished in the absence of PAR4 and supporting on-target drug activity. These studies demonstrate that PAR4 inhibition prolongs survival in female tumor-bearing mice but has no effect in males.

To ascertain whether the effects observed were specific to PAR4 and not an off-target effect of BMS986120, we transplanted tumor cells into PAR4-P322L, which have a 70% reduction in PAR4 function,[23] and PAR4$^{-/-}$ transgenic animals. Consistently, we observed that female PAR4-P322L mice had a longer survival when compared to wild-type animals, whereas we observed no difference in male PAR4-P322L mice (Figures 2H and 2I). This was further confirmed in the PAR4$^{-/-}$ model, where female PAR4$^{-/-}$ mice had a longer survival compared to wild-type female animals, with no difference in male PAR4$^{-/-}$ mice (Figures 2J and 2K).

Please cite this article in press as: Sloan et al., A sex-specific platelet switch controls anti-tumor immunity in glioblastoma, Cancer Cell (2026), https://doi.org/10.1016/j.ccell.2026.10.004

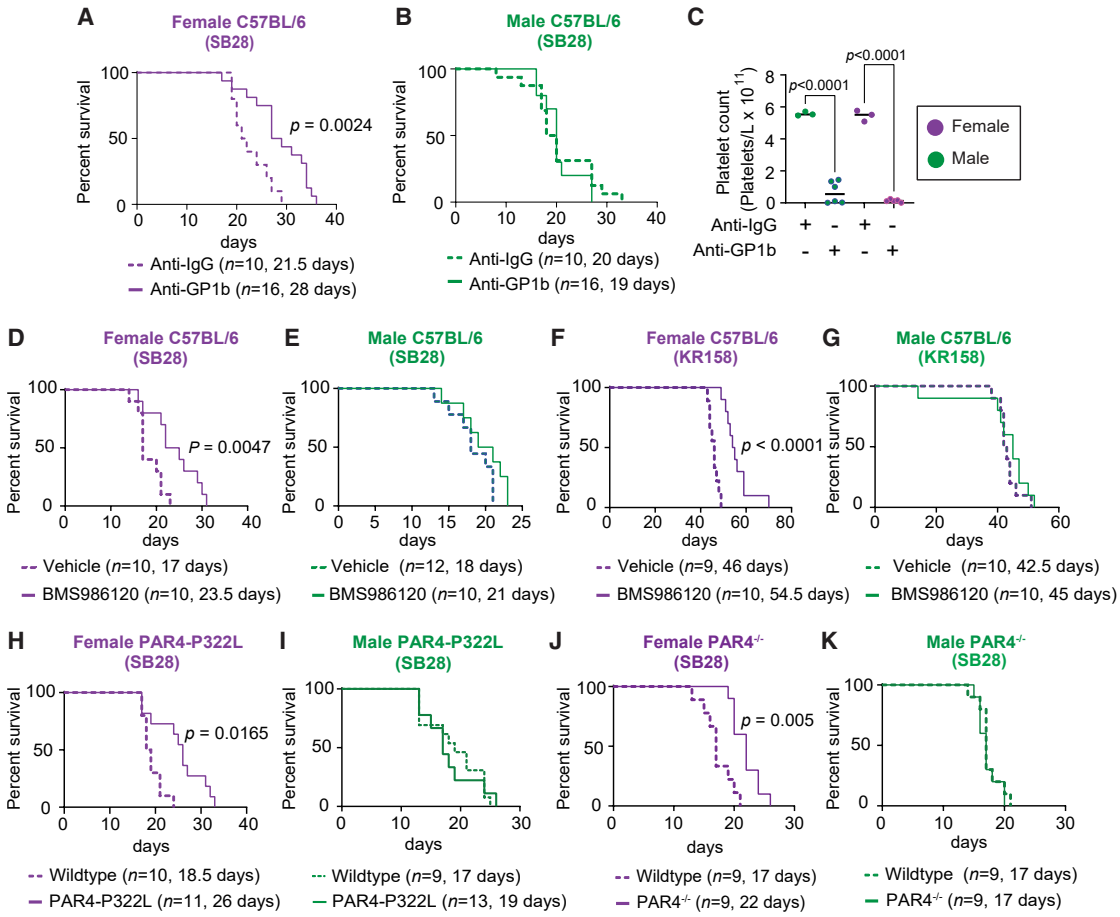


Figure 2. Inhibition of the thrombin-PAR4 signaling axis prolongs survival in a sex-dependent manner

(A and B) Kaplan-Meier survival analysis of C57BL/6 female (A) and male (B) mice following intracranial implantation of SB28 glioblastoma cells and treatment with an anti-GPIbα platelet-depleting antibody. *n* = 10/female IgG, *n* = 16/female anti-GP1b, *n* = 10/male IgG, *n* = 16/male anti-GP1b. Statistical significance was determined by log rank test.

(C) Complete blood count (CBC) platelet measurements obtained 1 day following anti-GPIbα administration to confirm platelet depletion in the animals shown in (A) and (B). Data are presented as each individual mouse mean ± SEM. *n* = 3/male IgG, *n* = 6/anti-GP1b; *n* = 3/female IgG, *n* = 5/female anti-GP1b. Statistical significance was determined by one-way ANOVA with Tukey's multiple-comparison test.

(D–G) Kaplan-Meier survival analysis of immunocompetent C57BL/6 mice implanted intracranially with SB28 (D and E) or KR158 (F and G) glioblastoma cells and treated with BMS986120 (2 mg/kg), a selective PAR4 antagonist. Statistical significance was determined by log rank test. SB28: *n* = 10/female vehicle, *n* = 10/female BMS986120, *n* = 12/male vehicle, *n* = 10/male BMS986120; KR158: *n* = 9/female vehicle, *n* = 10/female BMS986120, *n* = 10/male vehicle, *n* = 10/male BMS986120.

(H and I) Kaplan-Meier survival analysis comparing female (H) and male (I) wild-type and PAR4-P322L mice following intracranial implantation of SB28 glioblastoma cells. Statistical significance was determined by log rank test. *n* = 10/female wild-type, *n* = 10/female PAR4-P322L, *n* = 9/male wild-type, *n* = 13/male PAR4-P322L.

(J and K) Kaplan-Meier survival analysis comparing female (J) and male (K) wild-type and PAR4$^{-/-}$ mice following intracranial implantation of SB28 glioblastoma cells. Statistical significance was determined by log rank test. *n* = 9/female wild-type, *n* = 9/female PAR4$^{-/-}$, *n* = 10/male wild-type, *n* = 10/male PAR4$^{-/-}$.

Inhibiting the thrombin-PAR4 signaling axis prolongs survival in a female estrogen-dependent manner

To investigate the impact of sex chromosomes, sex hormones, and their interaction on the female survival advantage when the thrombin-PAR4 signaling axis is targeted, we utilized the four-core genotype mouse model, which separates the effects of sex chromosomes from gonadal hormones. Using this model, we observed that chromosomal male (XY), hormonal female mice exhibit a BMS986120-mediated survival advantage like that of wild-type females (Figures 3A and 3B), whereas chromosomal female (XX), hormonal male mice do not (Figures 3C and 3D). These results suggest that the survival advantage seen upon BMS986120 administration is dependent on female sex hormones. To further validate this hormone dependency, we performed ovariectomies on female mice. One month later, we intracranially implanted GBM cells and administered BMS986120. Estrogen depletion abolished any prior survival benefit observed with BMS986120 administration compared to sham-operation control mice (Figure 3E). Finally, to determine whether this was estrogen receptor specific, we utilized estrogen receptor β (ERβ) knockout (ERβ$^{-/-}$) mice to determine whether the female-specific survival benefit persisted in the absence of

Please cite this article in press as: Sloan et al., A sex-specific platelet switch controls anti-tumor immunity in glioblastoma, Cancer Cell (2026), https://doi.org/10.1016/j.ccell.2026.10.004

CellPress
OPEN ACCESS

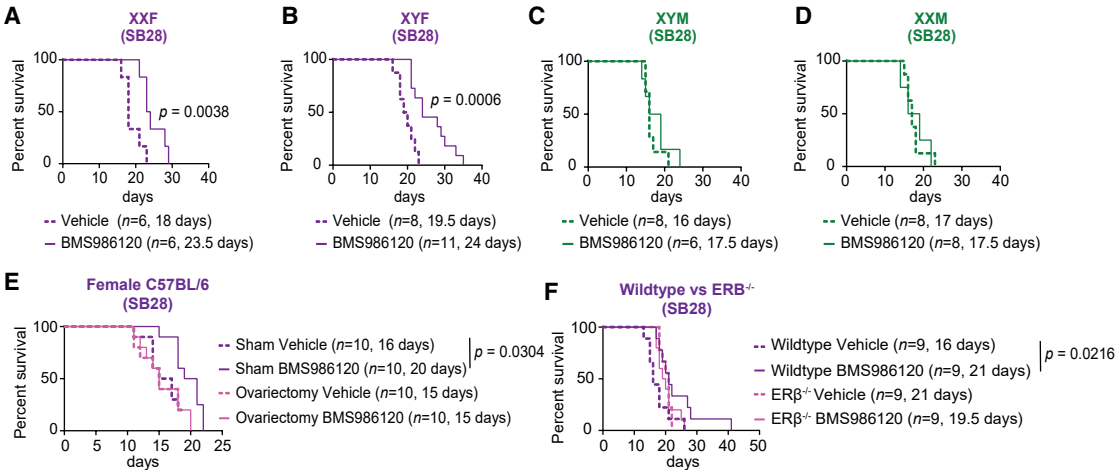


Figure 3. Inhibition of the thrombin-PAR4 signaling axis prolongs survival in an estrogen-dependent manner

(A–D) Kaplan-Meier survival analysis following intracranial implantation of SB28 glioblastoma cells and treatment with BMS986120. The four-core genotype model included (A) wild-type females, (B) chromosomal male (XY), hormonal female mice, (C) wild-type males, and (D) chromosomal female (XX), hormonal male mice. Statistical significance was determined by log rank test. n = 6/female wild-type vehicle, n = 6/female wild-type BMS986120, n = 8/chromosomal male (XY), hormonal female mice vehicle, n = 11/chromosomal male (XY), hormonal female mice BMS986120, n = 8/male wild-type vehicle, n = 6/male wild-type BMS986120, n = 8/chromosomal female (XX), hormonal male mice vehicle, n = 8/chromosomal female (XX), hormonal male mice BMS986120.

(E) Survival analysis of female C57BL/6 mice subjected to ovariectomy or sham surgery prior to intracranial implantation of SB28 cells and treatment with BMS986120 (2 mg/kg). Statistical significance was determined by log rank test. n = 10/sham vehicle, n = 10/sham BMS986120, n = 10/ovariectomy vehicle, n = 10/ovariectomy BMS986120.

(F) Kaplan-Meier survival analysis comparing female wild-type and ERβ$^{-/-}$ mice following intracranial implantation of SB28 glioblastoma cells. Statistical significance was determined by log rank test. n = 9/wild-type vehicle, n = 9/wild-type BMS986120, n = 9/ERβ$^{-/-}$ vehicle, n = 9/ERβ$^{-/-}$ BMS986120.

ERβ. Strikingly, genetic deletion of ERβ completely abolished the enhanced survival response to BMS986120 in female tumor-bearing mice (Figure 3F). These findings indicate that the female survival advantage is ERβ dependent and strongly support a model in which estrogen receptor signaling is required for the sex-specific effect of PAR4 inhibition.

ERβ interacts with PAR4 and regulates PAR4 signaling

To determine whether the estrogen-dependent survival advantage reflects direct transcriptional regulation of the F2RL3 (PAR4) gene, we treated MEG-01 megakaryocyte cells with β-estradiol, dihydrotestosterone, or progesterone and measured F2RL3 mRNA and PAR4 protein expression. Treatment with none of these hormones altered F2RL3 mRNA or PAR4 protein levels (Figures S6A–S6F), indicating that sex hormone signaling does not regulate PAR4 expression at the transcriptional level and prompting us to explore post-transcriptional and protein-interaction mechanisms."

Given that the female-specific survival benefit of PAR4 inhibition was ERβ dependent, we next asked whether ERβ directly influences PAR4. To address this, we examined PAR4 expression and its interaction with ERβ. Our immunofluorescence imaging of MEG-01 cells revealed co-expression of PAR4 and ERβ (Figure 4A), suggesting these two receptors may physically interact. Indeed, lysates immunoprecipitated with ERβ and probed for PAR4 (Figure 4B) or the reciprocal (Figure 4C) revealed that these proteins are in complex. However, lysates immunoprecipitated with ERα and probed for PAR4 revealed that PAR4 is not in a complex with ERα (Figure 4D). The PAR4-ERβ interaction was further confirmed by ERβ immunoprecipitation in human female platelets (Figure 4E) and human female brain microvascular endothelial cells (Figure 4F). These results support an interaction between ERβ and PAR4 in platelets and endothelial cells and suggest a mechanism that may underlie estrogen-dependent modulation of PAR4 signaling.

Next, we evaluated PAR4 signaling and its inhibition by BMS986120 in the presence of β-estradiol to determine whether estrogen induces estrogen receptor-dependent regulation of PAR4. Knowing that calcium signaling is downstream of PAR4, we used Fura-2 to image calcium and confirmed that PAR4 inhibition with BMS986120 suppresses Ca^{2+} signaling in MEG-01 cells, even when exposed to dihydrotestosterone (Figure 4G) or progesterone (Figure S6G). However, BMS986120 inhibition of PAR4 signaling was rescued when β-estradiol was present (Figure 4H). Additionally, utilizing a G protein-coupled receptor (GPCR) phospho-array, we found that estrogen preferentially promotes coordinated activation of calcium-enriched signaling pathways in MEG-01 cells, a response not observed with testosterone. Estrogen engaged ERβ-dependent signaling marked by increased phosphorylation of SRC and PYK2, in addition to modulation of MAPK and PI3K signaling components (Figures 4I–4M; Data S1), recapitulating the established ERβ-SRC-PYK2-PI3K platelet signaling axis and overlapping with PAR4-dependent calcium regulation. Estrogen exposure induced coherent activation of calcium-responsive kinases, including CAMK2β/γ/δ and CAMK4, preservation of integrin-associated proteins, and selective activation of PKC isoforms (Figures 4I–4M; Data S1), consistent with sustained intracellular Ca^{2+} flux. These upstream events converged on Ca^{2+}-linked MAPK intermediates, reflected by increased RSK and MSK phosphorylation, indicating engagement of the canonical CAMK-MAPK cascade. Together, these findings suggest that estrogen promotes a calcium-enriched GPCR signaling program in megakaryocytes.

Please cite this article in press as: Sloan et al., A sex-specific platelet switch controls anti-tumor immunity in glioblastoma, Cancer Cell (2026), https://doi.org/10.1016/j.ccell.2026.10.004

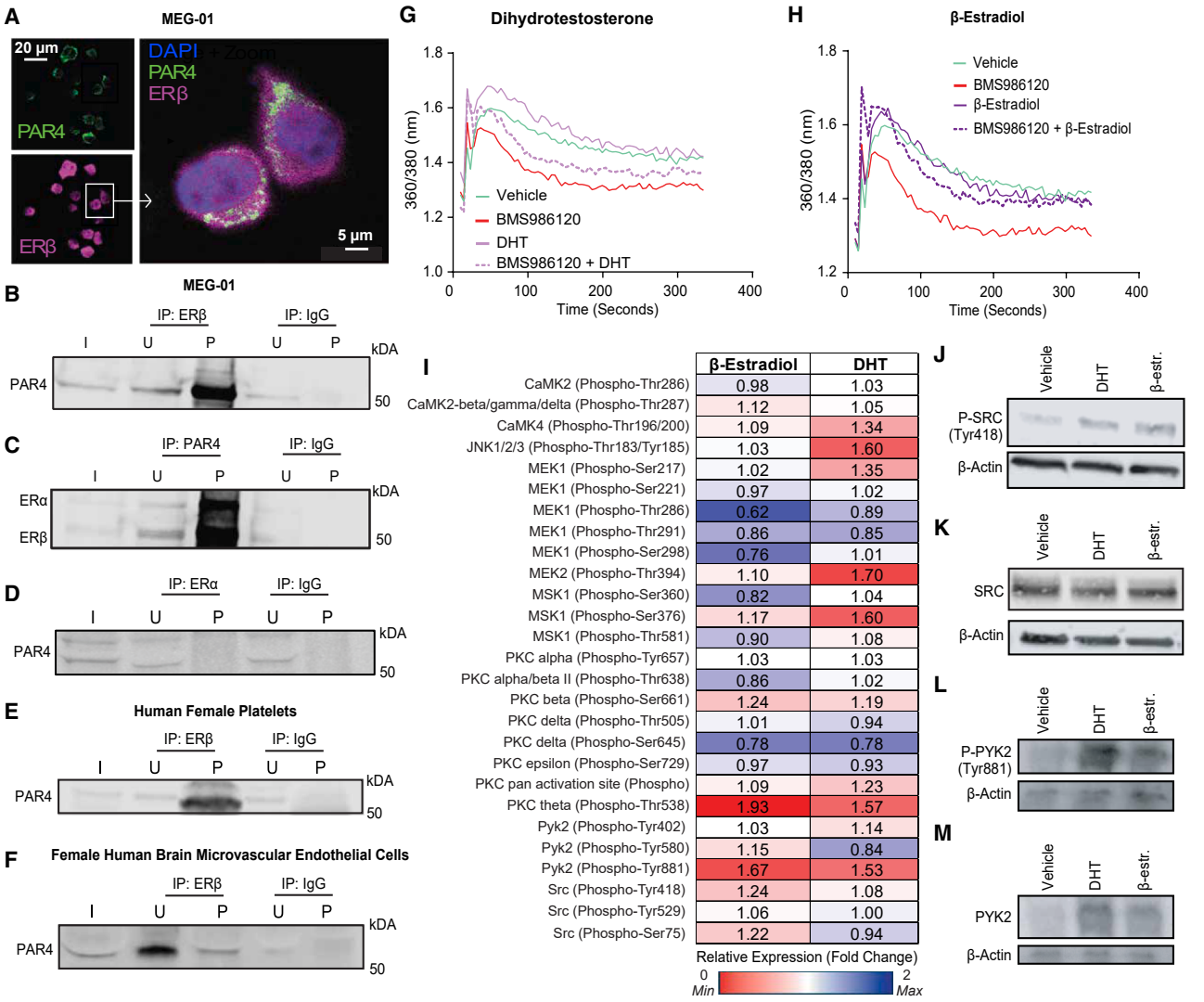


Figure 4. Estrogen receptor β interacts with and regulates PAR4 signaling

(A) Immunofluorescence staining of MEG-01 cells demonstrating expression of PAR4 and estrogen receptor β (ERβ). Representative merged image showing DAPI, PAR4, and ERβ staining.

(B) Immunoprecipitation of ERβ followed by immunoblotting for PAR4 in MEG-01 cells. I, input lysate; U, unbound fraction (post-immunoprecipitation supernatant); P, precipitated (immunoprecipitated) fraction.

(C) Immunoprecipitation of PAR4 followed by immunoblotting for ERβ and estrogen receptor α (ERα) in MEG-01 cells.

(D) Immunoprecipitation of ERα followed by immunoblotting for PAR4 in MEG-01 cells.

(E) Immunoprecipitation of ERβ followed by immunoblotting for PAR4 in human female platelets.

(F) Immunoprecipitation of PAR4 followed by immunoblotting for ERβ in human brain microvascular endothelial cells.

(G and H) Fura-2 calcium imaging of MEG-01 cells pretreated with BMS986120 and either dihydrotestosterone (G) or β-estradiol (H) followed by thrombin stimulation. Shown are representative traces/images from $n = 3$ independent experiments.

(I) G protein-coupled receptor (GPCR) phospho-array analysis of MEG-01 cells treated with β-estradiol or dihydrotestosterone for 4 consecutive days. Data are presented as fold change relative to vehicle-treated controls. Color scale represents normalized expression relative to MEG-01 cells that were vehicle treated (Min–Max; 0–2).

(J–M) Validation of GPCR phospho-array findings. MEG-01 cells treated with β-estradiol or dihydrotestosterone were analyzed by immunoblot for phospho-SRC (Tyr418) (J), SRC (K), phospho-PYK2 (Tyr881) (L), and PYK2 (M). Actin served as the loading control.

Inhibiting thrombin-PAR4 signaling enhances CD8$^+$ T cells in a sex-dependent manner

Based on these observations, we sought to determine the mechanism by which inhibiting the thrombin-PAR4 signaling axis prolongs survival in a sex-dependent manner. To determine whether the effect of BMS986120 was tumor cell intrinsic, we assessed proliferation in multiple murine GBM cell models treated with BMS986120 and observed no major differences in proliferation *in vitro* (Figures S7A and S7B), suggesting no significant impact on tumor cell fitness with BMS986120 treatment. These results

Please cite this article in press as: Sloan et al., A sex-specific platelet switch controls anti-tumor immunity in glioblastoma, Cancer Cell (2026), https://doi.org/10.1016/j.ccell.2026.10.004

CellPress
OPEN ACCESS

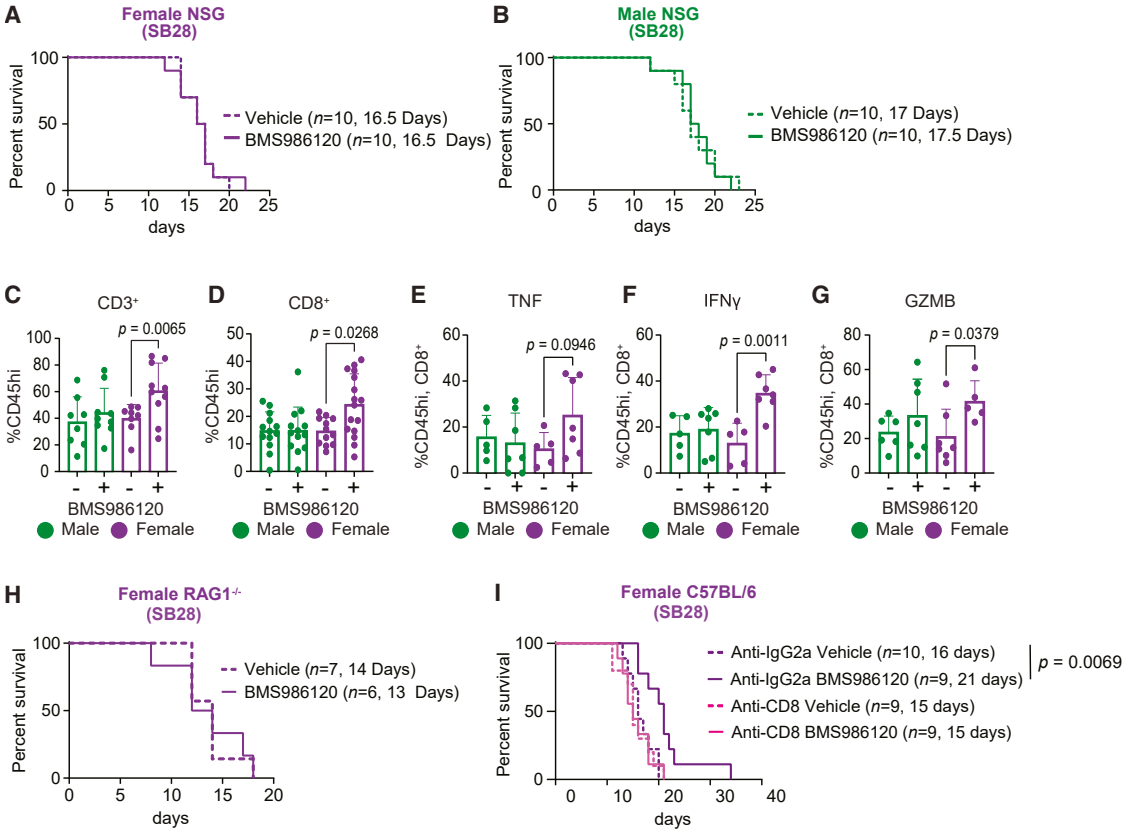


Figure 5. Inhibition of thrombin-PAR4 signaling enhances CD8$^+$ T cell responses in a sex-dependent manner

(A and B) Kaplan-Meier survival analysis of immunodeficient NSG mice bearing intracranial SB28 tumors and treated with BMS986120 (2 mg/kg). Statistical significance was determined by log rank test. *n* = 10/vehicle female, *n* = 10/female BMS986120, *n* = 10/male vehicle, *n* = 10/male BMS986120.

(C) Frequency of CD3$^+$ tumor-infiltrating T cell subsets 14 days after intracranial implantation of SB28 cells in male and female mice treated with vehicle or BMS986120. Data were combined from two independent experiments. Statistical significance was determined by one-way ANOVA with Tukey's multiple-comparison test. Data are presented as mean ± SEM. *n* = 8/male vehicle, *n* = 9/male BMS986120, *n* = 8/female vehicle, *n* = 10/female BMS986120.

(D) Frequency of CD8$^+$ tumor-infiltrating T cell subsets 14 days after intracranial implantation of SB28 cells in male and female mice treated with vehicle or BMS986120. Data were combined from two independent experiments. Statistical significance was determined by one-way ANOVA with Tukey's multiple-comparison test. Data are presented as mean ± SEM. *n* = 12/male vehicle, *n* = 13/male BMS986120, *n* = 12/female vehicle, *n* = 16/female BMS986120.

(E) Intracellular TNF expression in tumor-infiltrating CD8$^+$ T cells. Data were combined from two independent experiments. Statistical significance was determined by one-way ANOVA with Tukey's multiple-comparison test. Data are presented as mean ± SEM. *n* = 5/male vehicle, *n* = 7/male BMS986120, *n* = 5/female vehicle, *n* = 7/female BMS986120.

(F) Intracellular IFNγ expression in tumor-infiltrating CD8$^+$ T cells. Data were combined from two independent experiments. Statistical significance was determined by one-way ANOVA with Tukey's multiple-comparison test. Data are presented as mean ± SEM. *n* = 5/male vehicle, *n* = 7/male BMS986120, *n* = 5/female vehicle, *n* = 7/female BMS986120.

(G) Intracellular GZMB expression in tumor-infiltrating CD8$^+$ T cells. Data were combined from two independent experiments. Statistical significance was determined by one-way ANOVA with Tukey's multiple-comparison test. Data are presented as mean ± SEM. *n* = 6/male vehicle, *n* = 7/male BMS986120, *n* = 7/female vehicle, *n* = 5/female BMS986120.

(H) Kaplan-Meier survival analysis of SB28-bearing *Rag1*$^{-/-}$ female mice treated with BMS986120. Statistical significance was determined by log rank test. *n* = 7/vehicle, *n* = 6/BMS986120.

(I) Kaplan-Meier survival analysis of SB28-bearing female mice treated with anti-CD8-depleting antibody and BMS986120. Statistical significance was determined by log rank test. *n* = 10/anti-IgG2a vehicle, *n* = 9/anti-IgG2a BMS986120, *n* = 9/anti-CD8 vehicle, *n* = 9/anti-CD8 BMS986120.

led us to test whether the survival benefit seen in female tumor-bearing mice requires a fully functioning immune system. We intracranially transplanted NOD *scid* gamma (NSG) mice with murine GBM cells and subsequently inhibited PAR4 with BMS986120 administration. Pharmacologically inhibiting PAR4 with BMS986120 in immunodeficient mice did not show the survival benefit observed in immune-competent models (Figures 5A, 5B, S7C, and S7D). These findings suggest that the survival advantage observed in females when inhibiting the thrombin-PAR4 signaling axis depends on a functional immune system.

Platelets are known to influence immune cell function within the TME and in the systemic circulation.[13,24–27] While heterologous cell interactions are known to impact GBM, the question of whether platelets have sex-dependent effects is unexplored, and no studies have examined how PAR4 signaling regulates the TME across malignancies. To determine how the thrombin-PAR4 signaling axis contributes to the TME, we conducted

Please cite this article in press as: Sloan et al., A sex-specific platelet switch controls anti-tumor immunity in glioblastoma, Cancer Cell (2026), https://doi.org/10.1016/j.ccell.2026.10.004

immune profiling on tumor-infiltrating immune cells. We found that BMS986120-treated female mice had an increased percentage of CD45hi/CD3$^+$ cells, specifically CD45hi/CD8$^+$ tumor-infiltrating T cells 14 days post-tumor implantation (Figures 5C, 5D, and S7E; Table S5), with no changes in other T cell populations or exhaustion markers (Figures S8A–S8F). This BMS986120-mediated increase in CD8$^+$ T cells was also seen at 10 days post-BMS986120 treatment (Figures S9A and S9B; Table S5), but not at day 7 (Figures S9C and S9D; Table S5). Consistently, BMS986120-treated female CD8$^+$ T cells had an increase in cytokine expression upon *ex vivo* stimulation at day 14 (Figures 5E–5G; Table S6) but not at day 10 (Figures S10A–S10C; Table S6) or day 7 (Figures S10D–S10F; Table S6). There were no differences in other TME immune cell subsets (Figures S11A–S11E, S12A–S12H, S13, and S14; Table S7).

To further validate that the female survival benefit was CD8$^+$ T cell dependent, we intracranially transplanted GBM cells into *Rag1*$^{-/-}$ mice, which lack T and B cells, and treated with BMS986120. Removing T cells reversed the survival benefit observed when mice were treated with BMS986120 (Figure 5H); however, when regulatory T cells (Tregs) were removed by treating tumor-bearing *FoxP3-DTR* mice with BMS986120, female mice still exhibited a survival advantage (Figure S15A). To further isolate the effect specifically to CD8$^+$ T cells, we intracranially implanted murine GBM cells into C57BL/6 mice and administered anti-CD8 depletion antibody in combination with BMS986120. Depletion of CD8$^+$ T cells in the presence of BMS986120 completelyabolished the female survival benefit observed when the thrombin-PAR4 signaling axis was targeted (Figures 5I and S15B). Lastly, using multiplex immunofluorescence imaging, we demonstrated that BMS986120 results in a decrease in intratumoral platelet abundance (Figures 6A–6H and S16A–S16D) and an increase in cytotoxic CD8-expressing T cells in females, with no change in intratumoral platelets or CD8$^+$ T cells observed in male BMS986120-treated mice (Figures 6I–6M). Additionally, we saw no significant difference in other T cell or myeloid subsets (Figures S16E–S16G). Distance proximity analysis between platelets and CD8$^+$ T cells demonstrated trends where BMS986120 decreases the number of platelets in proximity to CD8$^+$ T cells in both males and females (Figure S16H). Taken together, our results suggest that the survival benefit of inhibiting thrombin-PAR4 signaling in GBM is sex dependent, driven by sex hormones, and mediated through a decrease in platelet interactions with CD8$^+$ T cells in the TME, supporting a platelet-immune mechanism underlying therapeutic outcomes.

PAR4 expression on platelets contributes to platelet-mediated immune suppression

PAR receptors, including PAR4, have been reported to be expressed on platelets, endothelial cells, and T cells,[28] implicating at least two potential mechanisms that could occur when PAR4 is targeted: a direct enhancement of CD8$^+$ T cells in females or the inhibition of PAR4 signaling on platelets, which then indirectly enhances CD8$^+$ T cell activity in females. We explored PAR transcriptional expression in human and mouse T cells by utilizing publicly available datasets and found that *F2rl3* was not expressed on T cells from mice (Figures S17A–S17D) and *F2RL3* was not expressed on T cells from humans (Figures S18A–S18D). However, mice (Figures S17A–S17D) and human (Figures S18A–S18D) T cells did express high levels of the PAR1 gene, *F2r* and *F2R*, respectfully. These results suggest that the increase in tumor-infiltrating CD8$^+$ T cells observed following PAR4 inhibition in females is unlikely from direct PAR4 signaling in T cells and that platelet signaling likely regulates tumor-infiltrating CD8$^+$ T cells in a sex-dependent manner via PAR4.

Using matched platelet and tumor samples from GBM patients, we observed that both platelets and tumor tissue exhibited high PAR4 expression, with no major differences in expression pattern between the two sources (Figures S19A–S19E). We subsequently performed immunohistochemical staining on GBM patient tissues to assess the cellular localization and distribution of PAR4 expression. Histological evaluation of H&E-stained tumor sections revealed numerous discrete round-to-oval, intensely dark-staining structures distributed throughout the tumor parenchyma. These structures varied in size, ranging from approximately 5- to 10-μm individual elements to larger clustered aggregates, and lacked visible nuclei (Figure S19F). Corresponding areas in PAR4-immunostained sections demonstrated positive brown DAB staining that was frequently associated with these same structures (Figures S19G–S19I). Based on their morphology and staining characteristics, these elements are most consistent with erythrocytes located within tumor-associated microvasculature and focal extravasated hemorrhagic regions. The findings are indicative of the abundant, abnormal neovasculature characteristic of GBM, with erythrocyte-filled microvessels and occasional microhemorrhagic foci distributed throughout the tumor tissue. PAR4 immunoreactivity was observed in association with these erythrocyte-rich vascular structures, consistent with PAR4 expression within components of the tumor vascular compartment (Figures S19G–S19I).

To investigate how platelets influence the immune landscape in human GBM, we generated a tissue microarray containing tumor regions with and without thrombosis (Figures S19J–S19U). Thrombotic regions were validated by elevated COL4A1 expression (Figures S19K and S19O). Analysis of immune cell infiltration demonstrated significantly greater immune cell accumulation in thrombosed compared with non-thrombosed GBM tissue (Figures S19L–S19N and S19P–S19U). This increase was primarily driven by CD11b$^+$ myeloid populations and CD4$^+$ T cells, whereas CD8$^+$ T cell infiltration was not higher in thrombotic regions (Figures S19Q, S19S, and S19T). Consistently, the CD4$^+$:CD8$^+$ T cell ratio was elevated in regions with thrombi, suggesting enhanced immune suppression in these regions (Figure S19U). Overall, matched analyses of GBM patient platelets and tumor tissue revealed similarly high and widespread PAR4 expression, while thrombotic tumor regions exhibited increased immune cell infiltration driven primarily by CD11b$^+$ myeloid cells and CD4$^+$ cells with an increased CD4$^+$:CD8$^+$ ratio consistent with a more immunosuppressive immune environment in regions containing thrombi.

Inhibiting PAR4 enhances platelet secretion and Ca^{2+} signaling in an estrogen-dependent manner

We next determined the mechanistic impact of pharmacologically inhibiting platelet PAR4 signaling on platelet function and

Please cite this article in press as: Sloan et al., A sex-specific platelet switch controls anti-tumor immunity in glioblastoma, Cancer Cell (2026), https://doi.org/10.1016/j.ccell.2026.10.004

CellPress
OPEN ACCESS

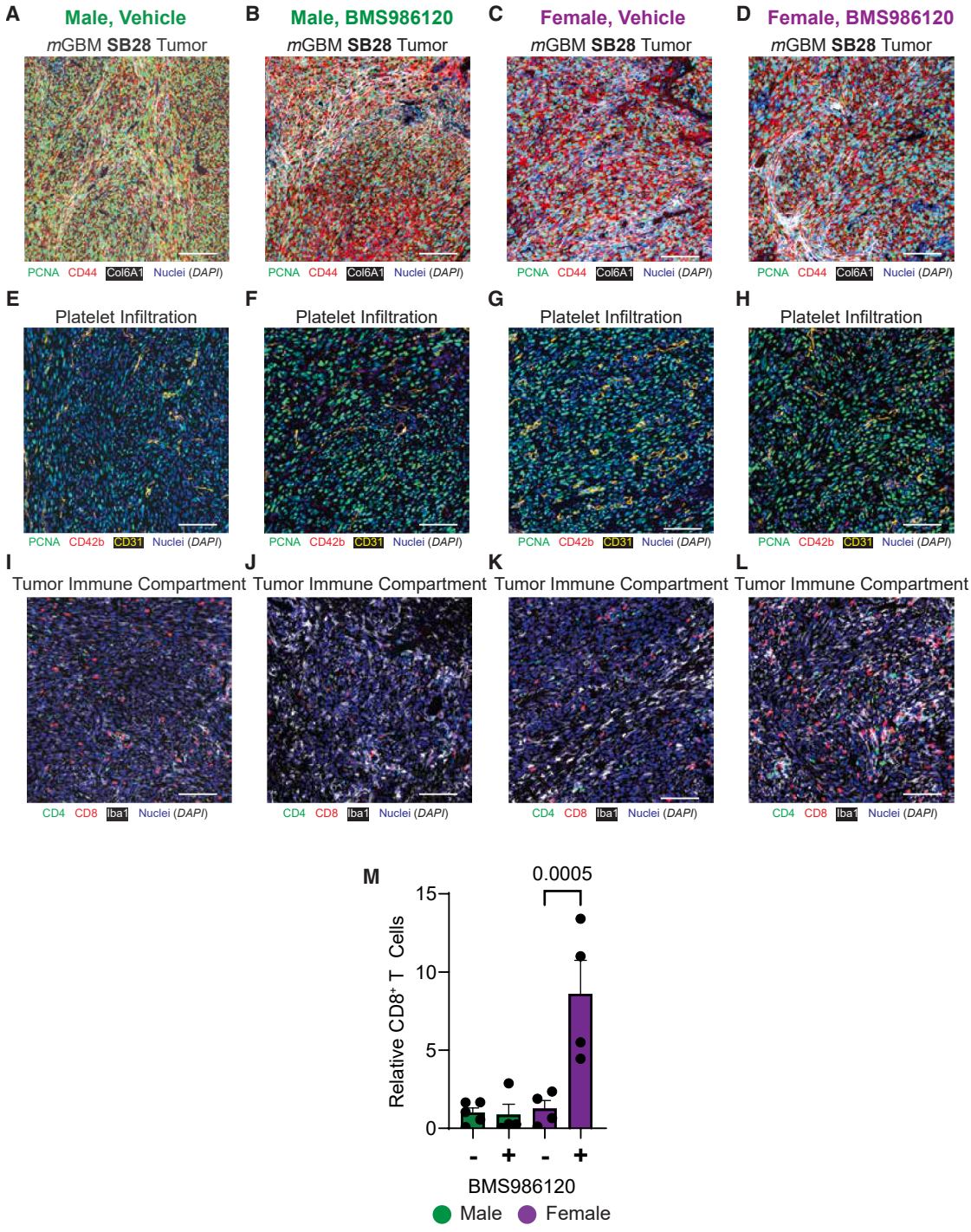


Figure 6. PAR4 inhibition increases intratumoral CD8⁺ T cells and decreases intratumoral platelet abundance in tumor-bearing mice

(A–D) Representative Akoya multiplex immunofluorescence images showing DAPI, PCNA, CD44, and COL6A1 staining in male vehicle-treated (A), male BMS986120-treated (B), female vehicle-treated (C), and female BMS986120-treated (D) tumors. Scale bars, 50 μm.

(E–H) Representative Akoya multiplex immunofluorescence images showing DAPI, CD42b, CD31, and PCNA staining in male vehicle-treated (E), male BMS986120-treated (F), female vehicle-treated (G), and female BMS986120-treated (H) tumors. Scale bars, 50 μm.

(I–L) Representative Akoya multiplex immunofluorescence images showing DAPI, CD4, CD8, and IBA1 staining in male vehicle-treated (I), male BMS986120-treated (J), female vehicle-treated (K), and female BMS986120-treated (L) tumors. Scale bars, 50 μm.

(M) Quantification of intratumoral CD8⁺ T cells in SB28-bearing male and female mice treated with vehicle or BMS986120. Statistical significance was determined by unpaired Student's *t* test. Data are presented as mean ± SEM from $n = 5$/vehicle female, $n = 4$/female BMS986120, $n = 4$/male vehicle, $n = 4$/male BMS986120.

Please cite this article in press as: Sloan et al., A sex-specific platelet switch controls anti-tumor immunity in glioblastoma, Cancer Cell (2026), https://doi.org/10.1016/j.ccell.2026.10.004

signaling in tumor-bearing mice. We initially isolated platelets from male and female control and tumor-bearing mice and treated them with BMS986120 *ex vivo*. Using flow cytometry, we found no differences in p-selectin and activated GPIIb/IIIa (JON/A) between tumor-bearing male and female platelets *ex vivo* (Figures S20A and S20B). These findings indicate that acute, *ex vivo* pharmacologic inhibition of PAR4 does not intrinsically alter platelet activation or α-granule secretion in a sex-dependent manner. The sex-specific effects of PAR4 inhibition observed *in vivo* therefore likely require the TME or sustained systemic signaling rather than direct platelet-intrinsic differences alone. Next, we intracranially transplanted GBM cells and treated mice with BMS986120 for 14 days. Aggregation assays demonstrated that pharmacologically inhibiting PAR4 had no effect on aggregation/thrombosis in tumor-bearing mice (Figure 7A). However, flow cytometry for p-selectin on platelets showed that female tumor-bearing mice had inhibited α-granule secretion following a 14-day treatment with BMS986120 (Figures 7B and S20C), whereas male mice treated with BMS986120 had no change in α-granule secretion (Figures 7C and S20D).

Proteomic Gene Ontology (GO) enrichment analysis demonstrated that peripheral platelets from BMS986120-treated female mice had enriched platelet degranulation and exocytosis signaling pathways (Figure 7D; Data S2). Additionally, the most highly enriched pathway in BMS986120-treated female mice was elevated platelet cytosolic Ca^{2+}. Consistently, GO enrichment analysis on vehicle-treated male and female tumor-bearing mice showed differences in several transport and exocytosis pathways, with no difference in elevated platelet cytosolic Ca^{2+} between male and female untreated platelets (Figure S20E; Data S2).

Calcium is essential for $CD8^+$ T cell activation, promoting their recruitment, cytokine production, and cytotoxic function through Ca^{2+}-dependent signaling pathways.[29] To address whether the enhanced Ca^{2+} signaling in female platelets when inhibiting PAR4 with BMS986120 is responsible for increased $CD8^+$ T cell function in the TME, we pre-treated platelets with the calcium release-activated calcium (CRAC) channel blocker YM-58483 or the calcium ionophore ionomycin. We found that pre-treatment of platelets with YM-58483 reduced $CD8^+$ T cell cytokine expression, whereas pre-treatment with ionomycin enhanced cytokine expression in $CD8^+$ T cells (Figures 7E–7H), with a more pronounced effect in females (Figures 7E and 7F) than in males (Figures 7G and 7H). Together, these results suggest that PAR4 inhibition enhances tumor-infiltrating $CD8^+$ T cells through a platelet-dependent, sex-dependent mechanism in which pharmacologic inhibition of PAR4 selectively alters calcium signaling and α-granule secretion in female platelets without affecting global aggregation.

Bidirectional regulation of functions between platelets and $CD8^+$ T cells in GBM

Our observations and previous work have demonstrated that high platelet counts associate with poor survival in GBM and multiple other malignancies.[4,30–33] Platelets also interact with and educate the function of other cells, including immune cells that have been identified in the TME and within the circulation.[13,24–27] However, the role of platelets in regulating the immunosuppressive TME remains poorly understood. When $CD8^+$ T cells were co-cultured with fresh platelets (provided daily), directly or using a Transwell, T cell function as measured by intracellular cytokine expression (Figures 8A, 8B, S20F, and S20G) and cytokine secretion (Figures 8C and 8D) was inhibited. When PAR4 function was decreased to 60% by using platelets from PAR4-P322L mice, this observed effect was reversed in female but not in male mice (Figures 8A and 8B). Additionally, inhibiting PAR4 with BMS986120 reversed the effect of platelets on cytokine secretion in females but not males (Figures 8C and 8D). In an *in vivo* setting, GBM tumor-bearing immunocompetent mice have constitutively higher platelet reactivity relative to their baseline. However, platelet hyperreactivity was not observed in tumor-bearing NSG mice, which lack T, B, and NK cells (Figure S20H). To further decipher whether tumor-induced platelet reactivity is T cell specific, GBM tumors were induced in *Rag1*$^{-/-}$ mice, which have no B or T cells. In this case, no increase in platelet reactivity was observed (Figure 8E). Consistently, we also tested platelet activity in tumor-bearing mice that were pretreated with an anti-CD8 antibody, and no enhanced platelet reactivity was found (Figure 8F). These results reveal that tumor-induced platelet reactivity in murine GBM models is dependent on the presence of immune cells, particularly $CD8^+$ T cells, and that subsequent $CD8^+$ T cell inhibition of platelets is dependent on PAR4.

DISCUSSION

Our study demonstrates a connection between platelet signaling, hormonal regulation, and immune activity within the GBM TME. Here, we show that GBM patients exhibit heightened platelet reactivity driven specifically by PAR4 signaling. In murine GBM models, both pharmacological inhibition of PAR4 using BMS986120 and genetic deletion of PAR4 significantly prolonged survival in females but not males. This survival advantage appears to be estrogen dependent: it is preserved in chromosomal male-hormonal female mice within the four-core genotype model and is abrogated in ovariectomized mice treated with estrogen. The survival benefit is associated with increased intratumoral $CD8^+$ T cell infiltration and requires an intact immune system. Inhibition of platelet PAR4 signaling increases calcium signaling through an estrogen-dependent interaction between PAR4 and ERβ.

Although BMS986120 reduced platelet-$CD8^+$ T cell proximity in both males and females, only females demonstrated a corresponding increase in intratumoral $CD8^+$ T cell accumulation. We speculate that this difference reflects estrogen-ERβ signaling in female platelets, which may uniquely couple thrombin-PAR4 inhibition to enhanced $CD8^+$ T cell recruitment and/or retention within the TME. Our findings support a model in which PAR4-activated platelets suppress $CD8^+$ T cell function within the TME, and depletion of $CD8^+$ T cells abolishes both the tumor-induced platelet reactivity and the survival benefit conferred by PAR4 inhibition. These effects are mediated through perturbations in immune function within the TME, driving sex-biased differences in immune cell subpopulations including microglia, MDSCs, and T cells.[8–10] This study suggests that cancer-associated thrombosis contributes to tumor progression, supporting precision medicine strategies that account for sex as a biological variable.

Please cite this article in press as: Sloan et al., A sex-specific platelet switch controls anti-tumor immunity in glioblastoma, Cancer Cell (2026), https://doi.org/10.1016/j.ccell.2026.10.004

CellPress
OPEN ACCESS

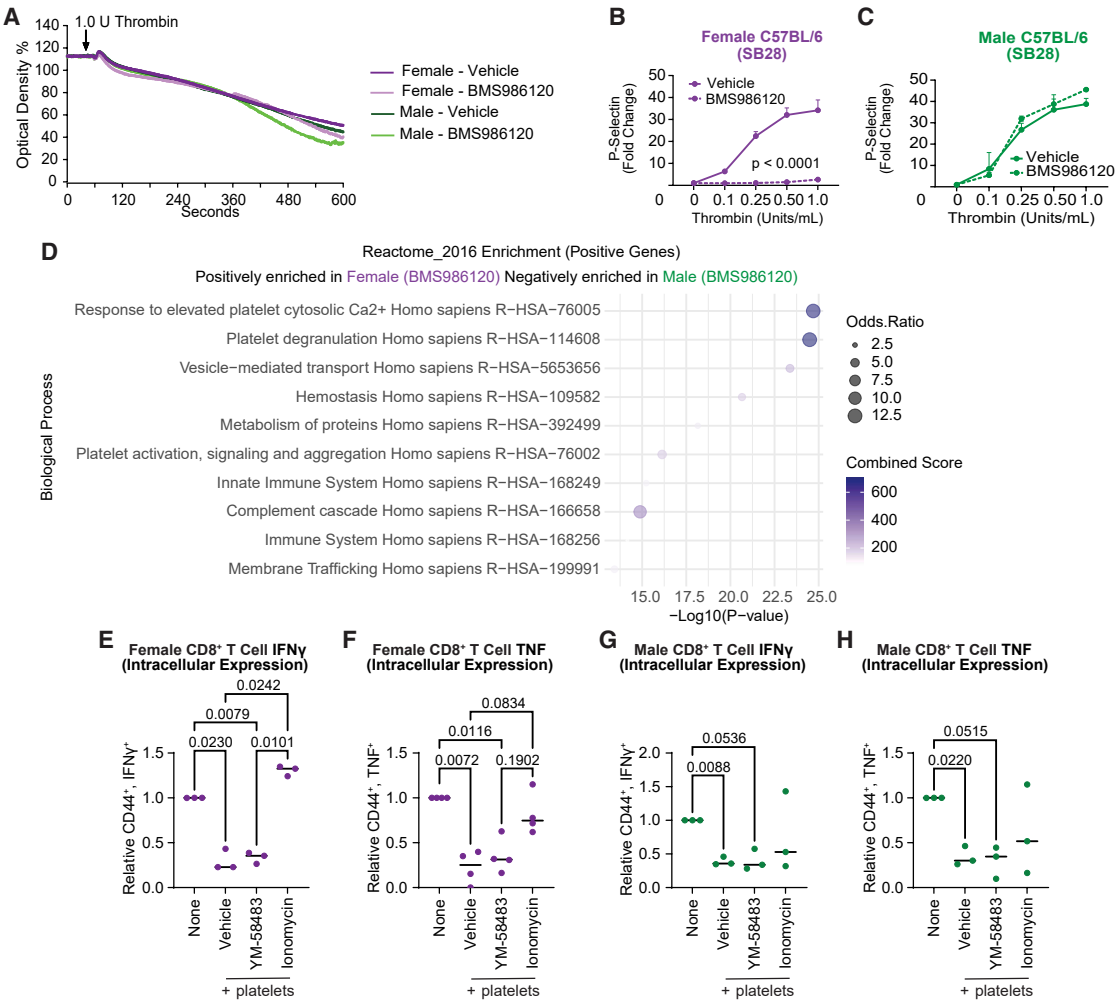


Figure 7. PAR4 inhibition enhances Ca^{2+} signaling, platelet secretion, and exocytosis in a sex-dependent manner

(A) Platelet aggregation analysis of washed platelets isolated from mice treated with BMS986120 following intracranial implantation of SB28 cells and stimulated with thrombin (1.0 Units/mL). Statistical significance was determined by two-way ANOVA. No statistically significant differences were observed between groups (all $p > 0.05$). Data are presented as mean, n = 3/vehicle female, n = 3/female BMS986120, n = 3/male vehicle, n = 3/male BMS986120.

(B and C) Washed platelets isolated from SB28-bearing mice treated with BMS986120 were analyzed for α-granule secretion by flow cytometry using a P-selectin-specific antibody. Data are presented as mean ± SEM from n = 4 independent experiments. Statistical significance was determined by two-way ANOVA.

(D) Gene Ontology enrichment analysis of platelet proteomic datasets from BMS986120-treated SB28-bearing mice. Positively enriched pathways represent pathways upregulated in female platelets relative to male platelets, whereas negatively enriched pathways represent pathways upregulated in male platelets relative to female platelets. Enrichment significance was assessed using Fisher's exact test and reported as adjusted p values. EnrichR combined scores were calculated by integrating the Fisher's exact test p value with a Z score reflecting deviation from the expected rank.

(E–H) Intracellular cytokine expression in $CD8^+$ T cells isolated from female (E and F) and male (G and H) C57BL/6 mouse spleens and co-cultured with sex-matched washed platelets. Platelets were pretreated with vehicle, YM-58483, or ionomycin prior to co-culture. Fresh platelets were added daily for 3 consecutive days. Intracellular IFNγ (E and G) and TNF (F and H) expression was measured by flow cytometry. Statistical significance was determined by one-way ANOVA with Tukey's multiple-comparison test. Data are presented as mean ± SEM from $n = 3$ (E, G, and H) and $n = 4$ (F) independent experiments. Statistical significance was determined by two-way ANOVA.

Cancer patients have a significantly higher risk of developing thrombotic events compared to the general population, with an estimated 9-fold increase in venous thromboembolism risk.[14,15,34,35] Recent studies highlight the role of platelet activation in the TME, where active platelets influence immune responses and promote pro-thrombotic conditions.[7] One likely source of thrombin in the GBM TME is the tumor cells themselves: we previously showed that cancer stem cells (CSCs) can endogenously produce all coagulation cascade components and generate biologically active thrombin locally—independent of plasma—providing a direct source within the tumor. In addition, thrombin in the TME could arise from: (1) expression of procoagulant factors (e.g., tissue factor) by tumor or stromal cells that drive local coagulation[16,36,37]; (2) disturbed or leaky tumor-associated vasculature, leading to plasma protein extravasation and local activation of coagulation; or (3) pro-coagulant

Please cite this article in press as: Sloan et al., A sex-specific platelet switch controls anti-tumor immunity in glioblastoma, Cancer Cell (2026), https://doi.org/10.1016/j.ccell.2026.10.004

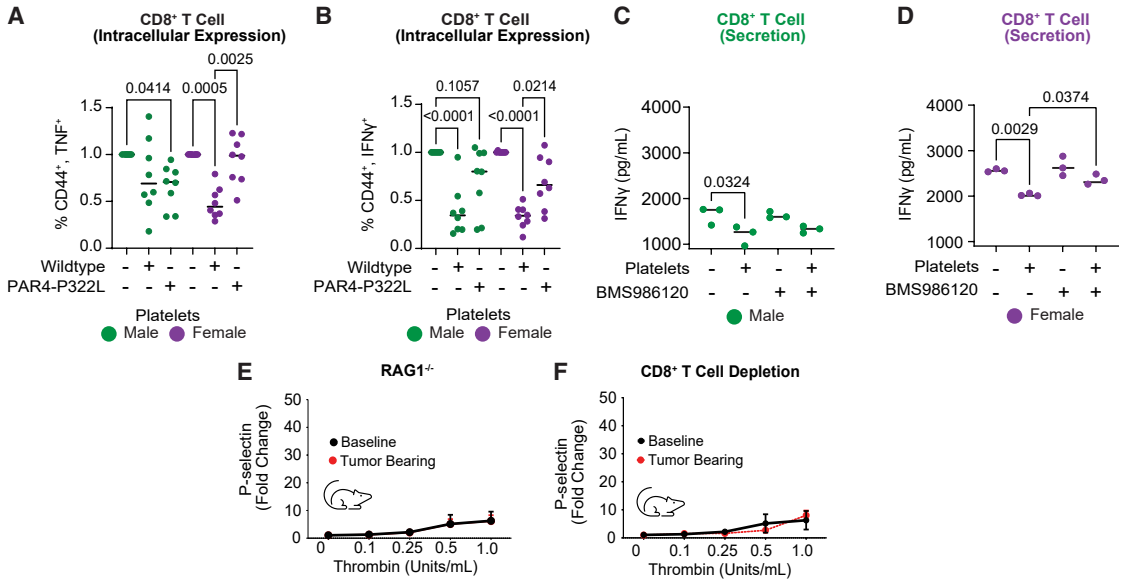


Figure 8. Bidirectional regulation between platelets and CD8$^+$ T cells in glioblastoma

(A and B) Intracellular cytokine expression in CD8$^+$ T cells isolated from C57BL/6 mouse spleens and co-cultured with sex-matched washed platelets isolated from wild-type or PAR4-P322L mice. Fresh platelets were added daily for 3 consecutive days. Intracellular TNF (A) and IFNγ (B) expression was measured by flow cytometry. Statistical significance was determined by one-way ANOVA with Tukey's multiple-comparison test. Data are presented as mean ± SEM. (A) $n = 8$ independent biological replicates per group.

(C and D) IFNγ secretion from male (C) and female (D) CD8$^+$ T cells isolated from C57BL/6 mouse spleens and co-cultured with sex-matched washed platelets. Fresh platelets were added daily for 3 consecutive days, and IFNγ levels in culture supernatants were quantified by ELISA. Statistical significance was determined by one-way ANOVA with Tukey's multiple-comparison test. Data are presented as mean ± SEM. $n = 3$ independent biological replicates per group.

(E and F) Washed platelets isolated from *Rag1*$^{-/-}$ mice (E) and CD8-depleted C57BL/6 mice (F) before intracranial tumor implantation (baseline) and 2 weeks after SB28 implantation. Washed platelets were stimulated with thrombin and platelet α-granule secretion was measured by flow cytometry using a P-selectin-specific antibody. Data are presented as mean ± SEM from $n = 4$ independent experiments.

extracellular vesicles or microparticles released by tumor, endothelial, or immune cells that catalyze thrombin generation. The broader phenomenon of tumor-driven coagulation activation via tissue factor and coagulation cascade components has been well described in solid cancers (and brain tumors).

Our work expands on this concept by demonstrating that tumor formation heightens platelet reactivity through PAR4, contributing to immune suppression in a sex-dependent manner and underscoring how tumors exploit normal physiological processes to create a microenvironment that supports tumor progression and survival. Our findings emphasize the importance of inhibiting cancer-associated thrombosis and platelet activation and suggest that, with further study, selective anticoagulation strategies might complement existing therapies and potentially enhance antitumor responses. Additionally, although this study focuses on GBM, the mechanistic coupling among platelet PAR4 signaling, thrombotic pathways, and immune modulation suggests broader relevance across cancers with high thrombotic burden. In addition to triple-negative breast cancer, these pathways may be particularly relevant in estrogen receptor-positive malignancies, where estrogen signaling could further intersect with platelet activation and immune regulation. Together, these observations raise the possibility that sex- and hormone-dependent PAR4 signaling may broadly influence antitumor immunity across cancer types with high thrombotic burden, including pancreatic, colon, and lung cancers, and warrant future investigation.

PAR4 inhibition may offer potential advantages over PAR1 inhibition due to its distinct signaling kinetics, which reduce bleeding risks while still effectively modulating platelet activity.[23,38,39] Unlike PAR1, which responds rapidly to low thrombin concentrations, PAR4 requires higher thrombin levels for activation, leading to more highly controlled platelet responses and minimizing excessive bleeding complications. Additionally, PAR4 mediates the prolonged signaling necessary for stable thrombus formation, whereas PAR1 activation results in a rapid, transient signal. By selectively inhibiting PAR4, therapeutic strategies may limit thrombosis while preserving essential hemostatic functions, reducing the likelihood of severe bleeding events associated with PAR1 inhibition.[23] Previous work has demonstrated that inhibiting PAR4 enhances CD4$^+$ T regulatory cells, contributing to immunosuppression[40]; however, our results show that PAR4 inhibition enhances CD8$^+$ T cell function in a sex-dependent manner. This could be because T cells in brain tumors often exhibit exhaustion, immunosuppression, and altered metabolism, which weaken their ability to effectively combat the tumor.[41] Compared to other tumor types, T cells in brain tumors face heightened challenges due to the brain's unique immune-privileged status and the suppressive TME, which includes factors such as regulatory T cells and tumor-associated macrophages.[42] These elements contribute to reduced T cell infiltration and impaired antitumor responses. These findings support further evaluation of PAR4 as a therapeutic target for platelet inhibition

Please cite this article in press as: Sloan et al., A sex-specific platelet switch controls anti-tumor immunity in glioblastoma, Cancer Cell (2026), https://doi.org/10.1016/j.ccell.2026.10.004

in cancer-associated thrombosis and other thrombotic disorders in females.

Limitations of the study

Our findings establish a mechanistic link between platelet PAR4 signaling, estrogen-ERβ interactions, and $CD8^+$ T cell-mediated immunity in preclinical GBM models; however, several important limitations should be considered. Translation to patients warrants caution, as human GBM is highly heterogeneous with respect to immune competence, treatment history, and hormonal status, all of which may influence platelet-immune interactions. Notably, postmenopausal women may exhibit increased estrogen receptor expression as a compensatory response to declining estrogen levels,[43] highlighting variability in ER signaling across patient populations.

From a translational perspective, these data suggest that PAR4 inhibition could benefit a subset of patients, particularly those with active estrogen-ERβ signaling and preserved antitumor immunity. However, therapeutic responses will likely depend on endocrine status, platelet activity, and concurrent treatments such as radiation and temozolomide, which can profoundly reshape the tumor microenvironment. These observations support the development of biomarker-driven patient stratification approaches that incorporate platelet function, ERβ signaling, and immune profiling to guide clinical evaluation of PAR4-targeted therapies.

Additional validation across diverse genetic backgrounds and clinically relevant GBM models will be necessary to establish the broader applicability of these findings. Although our data implicate estrogen as a key determinant of the survival benefit associated with PAR4 inhibition, the contributions of other hormonal pathways to platelet function and antitumor immunity remain unclear. Moreover, the impact of cyclical estrogen fluctuations on PAR4 expression and therapeutic efficacy was not examined in the present study. Because hormone-dependent regulation of PAR4 could influence treatment responsiveness, future studies integrating estrogen-driven dynamics can be leveraged to optimize PAR4-targeted interventions. The clinical potential of the PAR4 antagonist BMS986120 is encouraging; however, its long-term efficacy, safety profile, and potential off-target effects require further evaluation in both preclinical and clinical settings. Finally, although our results demonstrate that platelet-mediated suppression of $CD8^+$ T cell function occurs independently of direct cell-cell contact, the soluble mediators responsible for this effect remain unidentified. Future studies will be needed to define these factors and elucidate the molecular pathways through which platelets suppress antitumor T cell responses.

Based on our findings, future research is well positioned to investigate alternative platelet secretion mechanisms in shaping immune responses, with proteomic analyses identifying sex-specific signaling pathways that influence treatment efficacy. Examining how estrogen affects platelet-driven TME dynamics may yield hormone-modulating strategies to complement PAR4-targeted therapies. Expanding these insights into human studies and developing biomarkers for platelet activity could better predict patient outcomes. Our findings highlight the importance of addressing cancer-associated thrombosis and platelet activation as potential therapeutic targets and suggest that future studies should explore how anticoagulation strategies might interact with immune processes in GBM to improve patient outcomes.

RESOURCE AVAILABILITY

Lead contact

Requests for further information and resources should be directed to and will be fulfilled by the lead contact, Justin D. Lathia (lathiaj@ccf.org).

Materials availability

This study did not generate new unique reagents.

Data and code availability

Raw and processed data generated from the mouse platelet proteomics were uploaded to MassIVE (Mass Spectrometry Interaction Venue) and are available at the following link: https://doi.org/10.25345/C5VH5CZ89. Additionally, code and re-analyzed data used to generate analysis in this publication are available as follows: univariate Cox proportional hazards models, code available at https://github.com/andrewdhawan/par4-analysis-scripts; bulk RNA-seq and clinical data obtained from publicly available cohort data from The Cancer Genome Atlas Research Network[44] (Genomic Data Commons project accession: TCGA-GBM) and the China Glioma Genome Atlas[43] (CGGA mRNA-seq_325 and CGGA mRNAseq_693 [BioProject accession: PRJCA001747]); Mendelian analysis, code available at https://github.com/danielrosoff-ui/PAR4-GBM-MR, data from Ostrom et al.,[45] which combined four European-ancestry glioma GWAS, the Glioma International Case-Control Study (GICC) (GICC; dbGaP accession phs001319), the San Francisco Adult Glioma Study (SFAGS-GWAS) (SFAGS-GWAS; dbGaP accession phs001497), the MD Anderson Glioma GWAS (MDA-GWAS),[45,46] and the National Cancer Institute GliomaScan study (dbGaP accession phs000652); and publicly available single-cell analysis, code available at https://zenodo.org/records/21842910. Reference count matrices were obtained from 10× Genomics, including PBMCs from C57BL/6 mice (dataset accession pbmcs_1k_v1_mouse) and PBMCs from a Healthy Donor: Whole Transcriptome Analysis (dataset accession pbmcsca). Single-cell GBM datasets were obtained from the Glioblastoma Mapping Project (GBMap) and analyzed as previously described. All analyses were performed in R v.4.3.0. These resources are additionally listed in the key resources table under deposited data. Any additional information required to reanalyze the data reported in this paper is available from the lead contact upon request.

ACKNOWLEDGMENTS

We sincerely acknowledge the members of the Lathia laboratory for their valuable insights and constructive discussions and Dr. Reza Khatib for his inspiration and support of our work. We sincerely want to acknowledge Neal Restivo and Oatey Company for their support of our work. We are grateful for the illustrative contributions of Ms. Amanda Mendelsohn from Enterprise Creative at the Cleveland Clinic. We are grateful to Dr. Belinda Willard and her team at the Proteomics Core (RRID:SCR_026563) (Cleveland Clinic Research); Dr. Kewal Asosingh, PhD, and his team in the Flow Cytometry Core (RRID:SCR_026460) (Cleveland Clinic Research); Dr. Judith Draba, PhD, and her team at the Imaging Core (RRID:SCR_021852) (Cleveland Clinic Research); Carmel M. Burns and her team at the Cell Culture Core (RRID:SCR_026667) (Cleveland Clinic Research); and Drs. Charlie Androjna, D. Eng, and Dr. Timothy Myshrall, DVM, and their team in the Biological Resource Unit (Cleveland Clinic Research). Additionally, we extend our gratitude to Drs. Matthew Flick and Silvio Antoniak (University of North Carolina Chapel Hill) for their support and constructive comments on the project. This work was supported by NIH grants NIH T32 CA059366 (A.R.S.), F32 CA287655 (A.R.S.), R35 NS127083 (J.D.L.), P01 CA245705 (J.D.L. and J.B.R.), HL158801 (S.J.C.), U01HL143402 (A.A.K.), and R01HL164516 (A.A.K.). This work was also supported by the Cleveland Clinic VeloSano Bike to Cure event (S.J.C. and J.D.L.), Velosano 11 Pilot Grant (S.J.C.), and the Midwest Brain Tumor Foundation (A.R.S.), Cleveland Clinic (A.A.K. and J.D.L.) and Case Comprehensive Cancer Center (J.D.L.).

Please cite this article in press as: Sloan et al., A sex-specific platelet switch controls anti-tumor immunity in glioblastoma, Cancer Cell (2026), https://doi.org/10.1016/j.ccell.2026.10.004

AUTHOR CONTRIBUTIONS

Conception and design, A.R.S., S.J.C., and J.D.L.; development of methodology, A.R.S., G.B., A.A., and J.L.; acquisition of data, A.R.S., G.B., D.R., T.J.A., I.J., V.B., T.B., D.W., L.T., T.N., N.R., S.T.H., G.P.T., A.V., J.G., X.Y., S.K., J.C., V.S.K., S.S.K., A.S., B.R., N.S., and A.D.; analysis and interpretation of data: A.R.S., G.B., and J.L.; writing review, A.R.S., J.L., E.E.M.-H., J.B.R., C.M.O., S.J.C., and J.D.L.; administrative, technical, or material support, C.M.H., A.E.S., J.B.R., C.G.H., E.X.S., F.W.L., W.A.G., T.E.M., C.M.O., T.A.C., A.A.K., M.T.N., and A.D.; study supervision, S.J.C. and J.D.L.

DECLARATION OF INTERESTS

The authors declare no competing interests.

DECLARATION OF GENERATIVE AI AND AI-ASSISTED TECHNOLOGIES IN THE MANUSCRIPT PREPARATION PROCESS

During the preparation of this work, the authors used Microsoft copilot in order to validate and check grammar. After using this tool/service, the authors reviewed and edited the content as needed and take full responsibility for the content of the published article.

STAR★METHODS

Detailed methods are provided in the online version of this paper and include the following:

- KEY RESOURCES TABLE
- EXPERIMENTAL MODEL AND STUDY PARTICIPANT DETAILS
  - Human subjects
  - Mice
  - Cell models
- METHOD DETAILS
  - Intracranial tumor transplantation and treatments
  - Ovariectomy
  - Human platelet isolation and stimulation
  - Mouse platelet isolation and stimulation
  - Platelet light transmission aggregometry
  - Immunophenotyping by flow cytometry
  - *In vitro* $CD8^+$ T cell culture
  - MEG-01 cell culture experiments
  - Immunoblotting, antibodies, and GPCR phospho antibody array
  - Co-immunoprecipitation
  - Quantitative real-time PCR (qPCR)
  - MEG-01 calcium imaging
  - PAR4 immunohistochemistry
  - MEG-01 immunofluorescence
  - Assembly and testing of human cancer-associated thrombosis tissue microarray
  - Mouse platelet proteomics
  - Platelet gene signature analysis
  - Univariate Cox proportional hazards analysis
  - Analysis of previously published scRNA-seq data
  - Mendelian randomization analysis
  - Akoya multispectral immunofluorescence
- QUANTIFICATION AND STATISTICAL ANALYSIS

SUPPLEMENTAL INFORMATION

Supplemental information can be found online at https://doi.org/10.1016/j.ccell.2026.10.004.

Received: June 12, 2025
Revised: February 26, 2026
Accepted: October 7, 2026

REFERENCES

1. Xiao, T., Lee, J., Gauntner, T.D., Velegraki, M., Lathia, J.D., and Li, Z. (2024). Hallmarks of sex bias in immuno-oncology: mechanisms and therapeutic implications. Nat. Rev. Cancer *24*, 338–355. https://doi.org/10.1038/s41568-024-00680-z.
2. Ostrom, Q.T., Rubin, J.B., Lathia, J.D., Berens, M.E., and Barnholtz-Sloan, J.S. (2018). Females have the survival advantage in glioblastoma. Neuro Oncol. *20*, 576–577. https://doi.org/10.1093/neuonc/noy002.
3. Aggarwal, A., Jennings, C.L., Manning, E., and Cameron, S.J. (2023). Platelets at the Vessel Wall in Non-Thrombotic Disease. Circ. Res. *132*, 775–790. https://doi.org/10.1161/circresaha.122.321566.
4. Sloan, A.R., Lee-Poturalski, C., Hoffman, H.C., Harris, P.L., Elder, T.E., Richardson, B., Kerstetter-Fogle, A., Cioffi, G., Schroer, J., Desai, A., et al. (2022). Glioma stem cells activate platelets by plasma-independent thrombin production to promote glioblastoma tumorigenesis. Neurooncol. Adv. *4*, vdac172. https://doi.org/10.1093/noajnl/vdac172.
5. Liao, K., Zhang, X., Liu, J., Teng, F., He, Y., Cheng, J., Yang, Q., Zhang, W., Xie, Y., Guo, D., et al. (2023). The role of platelets in the regulation of tumor growth and metastasis: the mechanisms and targeted therapy. MedComm *4*, e350. https://doi.org/10.1002/mco2.350.
6. Sloan, A.R., Gordillo, A.J., Kennemer, A., Khorana, A.A., Horbinski, C., Kaelber, D.C., Cameron, S.J., and Lathia, J.D. (2025). Venous thromboembolism incidence shortens survival in isocitrate dehydrogenase wild-type glioblastoma. Neurooncol. Adv. *7*, vdaf018. https://doi.org/10.1093/noajnl/vdaf018.
7. Yang, J., Yamashita-Kanemaru, Y., Morris, B.I., Contursi, A., Trajkovski, D., Xu, J., Patrascan, I., Benson, J., Evans, A.C., Conti, A.G., et al. (2025). Aspirin prevents metastasis by limiting platelet TXA(2) suppression of T cell immunity. Nature *640*, 1052–1061. https://doi.org/10.1038/s41586-025-08626-7.
8. Turaga, S.M., Silver, D.J., Bayik, D., Paouri, E., Peng, S., Lauko, A., Alban, T.J., Borjini, N., Stanko, S., Naik, U.P., et al. (2020). JAM-A functions as a female microglial tumor suppressor in glioblastoma. Neuro Oncol. *22*, 1591–1601. https://doi.org/10.1093/neuonc/noaa148.
9. Bayik, D., Zhou, Y., Park, C., Hong, C., Vail, D., Silver, D.J., Lauko, A., Roversi, G., Watson, D.C., Lo, A., et al. (2020). Myeloid-Derived Suppressor Cell Subsets Drive Glioblastoma Growth in a Sex-Specific Manner. Cancer Discov. *10*, 1210–1225. https://doi.org/10.1158/2159-8290.Cd-19-1355.
10. Lee, J., Nicosia, M., Hong, E.S., Silver, D.J., Li, C., Bayik, D., Watson, D.C., Lauko, A., Kay, K.E., Wang, S.Z., et al. (2023). Sex-Biased T-cell Exhaustion Drives Differential Immune Responses in Glioblastoma. Cancer Discov. *13*, 2090–2105. https://doi.org/10.1158/2159-8290.Cd-22-0869.
11. Ostrom, Q.T., Kinnersley, B., Wrensch, M.R., Eckel-Passow, J.E., Armstrong, G., Rice, T., Chen, Y., Wiencke, J.K., McCoy, L.S., Hansen, H.M., et al. (2018). Sex-specific glioma genome-wide association study identifies new risk locus at 3p21.31 in females, and finds sex-differences in risk at 8q24.21. Sci. Rep. *8*, 7352. https://doi.org/10.1038/s41598-018-24580-z.
12. Lee, J., Chung, Y.M., Silver, D.J., Hao, Y., Harwood, D.S.L., Ealy, A., Serapiglia, A.M., Curtin, L., Benedetti, J.R., Ballard, C.A.P., et al. (2026). Androgen loss accelerates brain tumour growth via HPA axis activation. Nature *653*, 1184–1195. https://doi.org/10.1038/s41586-026-10451-5.
13. Fomchenko, E.I., and Holland, E.C. (2007). Platelet-derived growth factor-mediated gliomagenesis and brain tumor recruitment. Neurosurg. Clin. N. Am. *18*, 39–58. https://doi.org/10.1016/j.nec.2006.10.006.
14. Khorana, A.A., Mackman, N., Falanga, A., Pabinger, I., Noble, S., Ageno, W., Moik, F., and Lee, A.Y.Y. (2022). Cancer-associated venous thromboembolism. Nat. Rev. Dis. Primers *8*, 11. https://doi.org/10.1038/s41572-022-00336-y.
15. Wang, T.F., Khorana, A.A., Agnelli, G., Bloomfield, D., Bonaca, M.P., Büller, H.R., Connors, J.M., Goto, S., Jing, Z.C., Kakkar, A.K., et al. (2023). Treatment of Cancer-Associated Thrombosis: Recent Advances,

Please cite this article in press as: Sloan et al., A sex-specific platelet switch controls anti-tumor immunity in glioblastoma, Cancer Cell (2026), https://doi.org/10.1016/j.ccell.2026.10.004

Unmet Needs, and Future Direction. Oncologist *28*, 555–564. https://doi.org/10.1093/oncolo/oyad116.

16. Burdett, K.B., Unruh, D., Drumm, M., Steffens, A., Lamano, J., Judkins, J., Schwartz, M., Javier, R., Amidei, C., Lipp, E.S., et al. (2023). Determining venous thromboembolism risk in patients with adult-type diffuse glioma. Blood *141*, 1322–1336. https://doi.org/10.1182/blood.2022017858.
17. Diaz, M., Jo, J., Smolkin, M., Ratcliffe, S.J., and Schiff, D. (2021). Risk of Venous Thromboembolism in Grade II-IV Gliomas as a Function of Molecular Subtype. Neurology *96*, e1063–e1069. https://doi.org/10.1212/wnl.0000000000011414.
18. Unruh, D., and Horbinski, C. (2020). Beyond thrombosis: the impact of tissue factor signaling in cancer. J. Hematol. Oncol. *13*, 93. https://doi.org/10.1186/s13045-020-00932-z.
19. Suzuki, K., Aiura, K., Kitagou, M., Hoshimoto, S., Takahashi, S., Ueda, M., and Kitajima, M. (2004). Platelets counts closely correlate with the disease-free survival interval of pancreatic cancer patients. Hepatogastroenterology *51*, 847–853.
20. Lin, M.S., Huang, J.X., Zhu, J., and Shen, H.Z. (2012). Elevation of platelet count in patients with colorectal cancer predicts tendency to metastases and poor prognosis. Hepatogastroenterology *59*, 1687–1690. https://doi.org/10.5754/hge12277.
21. Kornblith, L.Z., Bainton, C.M.V., Fields, A.T., Matthay, Z.A., Magid, N.T., Nunez-Garcia, B., Prakash, A., Kurien, P.A., Callcut, R.A., Cohen, M.J., and Bainton, R.J. (2020). A journey upstream: Fluctuating platelet-specific genes in cell-free plasma as proof-of-concept for using ribonucleic acid sequencing to improve understanding of postinjury platelet biology. J. Trauma Acute Care Surg. *88*, 742–751. https://doi.org/10.1097/ta.0000000000002681.
22. Cooke, N.M., Egan, K., McFadden, S., Grogan, L., Breathnach, O.S., O'Leary, J., Hennessy, B.T., and Kenny, D. (2013). Increased platelet reactivity in patients with late-stage metastatic cancer. Cancer Med. *2*, 564–570. https://doi.org/10.1002/cam4.86.
23. Han, X., Knauss, E.A., Fuente, M.D.L., Li, W., Conlon, R.A., LePage, D.F., Jiang, W., Renna, S.A., McKenzie, S.E., and Nieman, M.T. (2024). A mouse model of the protease-activated receptor 4 Pro310Leu variant has reduced platelet reactivity. J. Thromb. Haemostasis *22*, 1715–1726. https://doi.org/10.1016/j.jtha.2024.03.004.
24. In 't Veld, S.G.J.G., and Wurdinger, T. (2019). Tumor-educated platelets. Blood *133*, 2359–2364. https://doi.org/10.1182/blood-2018-12-852830.
25. Verheul, H.M.W., Jorna, A.S., Hoekman, K., Broxterman, H.J., Gebbink, M.F.B.G., and Pinedo, H.M. (2000). Vascular endothelial growth factor-stimulated endothelial cells promote adhesion and activation of platelets. Blood *96*, 4216–4221. https://doi.org/10.1182/blood.v96.13.4216.h8004216_4216_4221.
26. Nash, G.F., Turner, L.F., Scully, M.F., and Kakkar, A.K. (2002). Platelets and cancer. Lancet Oncol. *3*, 425–430. https://doi.org/10.1016/s1470-2045(02)00789-1.
27. Pinedo, H.M., Verheul, H.M., D'Amato, R.J., and Folkman, J. (1998). Involvement of platelets in tumour angiogenesis? Lancet *352*, 1775–1777. https://doi.org/10.1016/s0140-6736(98)05095-8.
28. Shpacovitch, V., Feld, M., Hollenberg, M.D., Luger, T.A., and Steinhoff, M. (2008). Role of protease-activated receptors in inflammatory responses, innate and adaptive immunity. J. Leukoc. Biol. *83*, 1309–1322. https://doi.org/10.1189/jlb.0108001.
29. Hogan, P.G., Lewis, R.S., and Rao, A. (2010). Molecular basis of calcium signaling in lymphocytes: STIM and ORAI. Annu. Rev. Immunol. *28*, 491–533. https://doi.org/10.1146/annurev.immunol.021908.132550.
30. Williams, M., Liu, Z.W., Woolf, D., Hargreaves, S., Michalarea, V., Menashy, R., Kooner, I., and Wilson, E. (2012). Change in platelet levels during radiotherapy with concurrent and adjuvant temozolomide for the treatment of glioblastoma: a novel prognostic factor for survival. J. Cancer Res. Clin. Oncol. *138*, 1683–1688. https://doi.org/10.1007/s00432-012-1243-x.
31. Takemoto, A., Okitaka, M., Takagi, S., Takami, M., Sato, S., Nishio, M., Okumura, S., and Fujita, N. (2017). A critical role of platelet TGF-β release in podoplanin-mediated tumour invasion and metastasis. Sci. Rep. *7*, 42186. https://doi.org/10.1038/srep42186.
32. Midorikawa, Y., Takayama, T., Higaki, T., Aramaki, O., Teramoto, K., Yoshida, N., Tsuji, S., Kanda, T., and Moriyama, M. (2020). High platelet count as a poor prognostic factor for liver cancer patients without cirrhosis. Biosci. Trends *14*, 368–375. https://doi.org/10.5582/bst.2020.03230.
33. Baranyai, Z., Jósa, V., Tóth, A., Szilasi, Z., Tihanyi, B., Zaránd, A., Harsanyi, L., and Szállási, Z. (2016). Paraneoplastic thrombocytosis in gastrointestinal cancer. Platelets *27*, 269–275. https://doi.org/10.3109/09537104.2016.1170112.
34. Wan, T., Song, J., and Zhu, D. (2025). Cancer-associated venous thromboembolism: a comprehensive review. Thromb. J. *23*, 35. https://doi.org/10.1186/s12959-025-00719-7.
35. Wang, T.F., Li, A., and Garcia, D. (2018). Managing thrombosis in cancer patients. Res. Pract. Thromb. Haemost. *2*, 429–438. https://doi.org/10.1002/rth2.12102.
36. Magnus, N., Garnier, D., and Rak, J. (2010). Oncogenic epidermal growth factor receptor up-regulates multiple elements of the tissue factor signaling pathway in human glioma cells. Blood *116*, 815–818. https://doi.org/10.1182/blood-2009-10-250639.
37. Tawil, N., Bassawon, R., Meehan, B., Nehme, A., Montermini, L., Gayden, T., De Jay, N., Spinelli, C., Chennakrishnaiah, S., Choi, D., et al. (2021). Glioblastoma cell populations with distinct oncogenic programs release podoplanin as procoagulant extracellular vesicles. Blood Adv. *5*, 1682–1694. https://doi.org/10.1182/bloodadvances.2020002998.
38. Künze, G., and Isermann, B. (2023). Targeting biased signaling by PAR1: function and molecular mechanism of parmodulins. Blood *141*, 2684. https://doi.org/10.1182/blood.2023019775.
39. Li, S., Wang, W., Lin, L., Yang, L., Cai, Y., Yang, X., Zhang, T., Xiao, C., Yan, H., Gao, N., and Zhao, J. (2023). Oligosaccharide Blocks PAR1 (Proteinase-Activated Receptor 1)-PAR4-Mediated Platelet Activation by Binding to Thrombin Exosite II and Impairs Thrombosis. Arterioscler. Thromb. Vasc. Biol. *43*, 253–266. https://doi.org/10.1161/atvbaha.122.318085.
40. Bock, M., Bergmann, C.B., Jung, S., Biberthaler, P., Heimann, L., and Hanschen, M. (2022). Platelets differentially modulate CD4(+) Treg activation via GPIIa/IIIb-fibrinogen-and PAR4-dependent pathways. Immunol. Res. *70*, 185–196. https://doi.org/10.1007/s12026-021-09258-5.
41. Mohme, M., and Neidert, M.C. (2020). Tumor-Specific T Cell Activation in Malignant Brain Tumors. Front. Immunol. *11*, 205. https://doi.org/10.3389/fimmu.2020.00205.
42. Yang, W., Liu, S., Mao, M., Gong, Y., Li, X., Lei, T., Liu, C., Wu, S., and Hu, Q. (2024). T-cell infiltration and its regulatory mechanisms in cancers: insights at single-cell resolution. J. Exp. Clin. Cancer Res. *43*, 38. https://doi.org/10.1186/s13046-024-02960-w.
43. Zhao, Z., Zhang, K.N., Wang, Q., Li, G., Zeng, F., Zhang, Y., Wu, F., Chai, R., Wang, Z., Zhang, C., et al. (2021). Chinese Glioma Genome Atlas (CGGA): A Comprehensive Resource with Functional Genomic Data from Chinese Glioma Patients. Genom. Proteom. Bioinform. *19*, 1–12. https://doi.org/10.1016/j.gpb.2020.10.005.
44. The Cancer Genome Atlas Research Network (2008). Comprehensive genomic characterization defines human glioblastoma genes and core pathways. Nature *455*, 1061–1068. https://doi.org/10.1038/nature07385.
45. Ostrom, Q.T., Kinnersley, B., Armstrong, G., Rice, T., Chen, Y., Wiencke, J.K., McCoy, L.S., Hansen, H.M., Amos, C.I., Bernstein, J.L., et al. (2018). Age-specific genome-wide association study in glioblastoma identifies increased proportion of 'lower grade glioma'-like features associated with younger age. Int. J. Cancer *143*, 2359–2366. https://doi.org/10.1002/ijc.31759.
46. Melin, B.S., Barnholtz-Sloan, J.S., Wrensch, M.R., Johansen, C., Il'yasova, D., Kinnersley, B., Ostrom, Q.T., Labreche, K., Chen, Y., Armstrong, G., et al. (2017). Genome-wide association study of glioma

Please cite this article in press as: Sloan et al., A sex-specific platelet switch controls anti-tumor immunity in glioblastoma, Cancer Cell (2026), https://doi.org/10.1016/j.ccell.2026.10.004

subtypes identifies specific differences in genetic susceptibility to glioblastoma and non-glioblastoma tumors. Nat. Genet. *49*, 789–794. https://doi.org/10.1038/ng.3823.

47. Mumaw, M.M., de la Fuente, M., Arachiche, A., Wahl, J.K., 3rd, and Nieman, M.T. (2015). Development and characterization of monoclonal antibodies against Protease Activated Receptor 4 (PAR4). Thromb. Res. *135*, 1165–1171. https://doi.org/10.1016/j.thromres.2015.03.027.
48. Ma, J., Shi, Y., Lu, Q., and Huang, D. (2024). F2RL3 Regulates Epithelial-Mesenchymal Transition and Angiogenesis in Gastric Cancer through the Rap1/MAPK Signaling Pathway. Front. Biosci. *29*, 177. https://doi.org/10.31083/j.fbl2905177.
49. Goldsborough, T., Philps, B., O'Callaghan, A., Inglis, F., Leplat, L., Filby, A., Bilen, H., and Bankhead, P. (2024). InstanSeg: an embedding-based instance segmentation algorithm optimized for accurate, efficient and portable cell segmentation. Preprint at arXiv.
50. Rumberger, J.L., Greenwald, N.F., Ranek, J.S., Boonrat, P., Walker, C., Franzen, J., Varra, S.R., Kong, A., Sowers, C., Liu, C.C., et al. (2025). Automated classification of cellular expression in multiplexed imaging data with Nimbus. Nat. Methods *22*, 2161–2170. https://doi.org/10.1038/s41592-025-02826-9.
51. Van Gassen, S., Callebaut, B., Van Helden, M.J., Lambrecht, B.N., Demeester, P., Dhaene, T., and Saeys, Y. (2015). FlowSOM: Using self-organizing maps for visualization and interpretation of cytometry data. Cytometry A *87*, 636–645. https://doi.org/10.1002/cyto.a.22625.
52. Bankhead, P., Loughrey, M.B., Fernández, J.A., Dombrowski, Y., McArt, D.G., Dunne, P.D., McQuaid, S., Gray, R.T., Murray, L.J., Coleman, H.G., et al. (2017). QuPath: Open source software for digital pathology image analysis. Sci. Rep. *7*, 16878. https://doi.org/10.1038/s41598-017-17204-5.
53. Morrell, C.N., Mix, D., Aggarwal, A., Bhandari, R., Godwin, M., Owens, P., III, Lyden, S.P., Doyle, A., Krauel, K., Rondina, M.T., et al. (2022). Platelet olfactory receptor activation limits platelet reactivity and growth of aortic aneurysms. J. Clin. Investig. *132*, e152373. https://doi.org/10.1172/jci152373.
54. Godwin, M.D., Aggarwal, A., Hilt, Z., Shah, S., Gorski, J., and Cameron, S.J. (2022). Sex-Dependent Effect of Platelet Nitric Oxide: Production and Platelet Reactivity in Healthy Individuals. JACC, Basic Transl. Sci. *7*, 14–25. https://doi.org/10.1016/j.jacbts.2021.10.009.
55. Mulkearns-Hubert, E.E., Hajdari, N., Hong, E.S., Jacobs, A.P., Gaboriau, A., Giltner, S., Tannish, G., Kay, K.E., Wang, S.Z., LaViolette, P.S., et al. (2025). Connexin 43 drives glioblastoma cancer stem cell phenotypes through a WNK lysine-deficient protein kinase 1-c-MYC signaling axis. Cell Rep. *44*, 116303. https://doi.org/10.1016/j.celrep.2025.116303.
56. Baruah, V., and O'Connor, C.M. (2025). The BTK-DDX41 axis of the STING pathway is activated during cytomegalovirus lytic infection. J. Virol. *99*, e0104825. https://doi.org/10.1128/jvi.01048-25.
57. Kuleshov, M.V., Jones, M.R., Rouillard, A.D., Fernandez, N.F., Duan, Q., Wang, Z., Koplev, S., Jenkins, S.L., Jagodnik, K.M., Lachmann, A., et al. (2016). Enrichr: a comprehensive gene set enrichment analysis web server 2016 update. Nucleic Acids Res. *44*, W90–W97. https://doi.org/10.1093/nar/gkw377.
58. Hao, Y., Hao, S., Andersen-Nissen, E., Mauck, W.M., 3rd, Zheng, S., Butler, A., Lee, M.J., Wilk, A.J., Darby, C., Zager, M., et al. (2021). Integrated analysis of multimodal single-cell data. Cell *184*, 3573–3587.e29. https://doi.org/10.1016/j.cell.2021.04.048.
59. Ruiz-Moreno, C., Salas, S.M., Samuelsson, E., Minaeva, M., Ibarra, I., Grillo, M., Brandner, S., Roy, A., Forsberg-Nilsson, K., Kranendonk, M.E.G., et al. (2025). Charting the single-cell and spatial landscape of IDH-wild-type glioblastoma with GBmap. Neuro Oncol. *27*, 2281–2295. https://doi.org/10.1093/neuonc/noaf113.
60. Vuckovic, D., Bao, E.L., Akbari, P., Lareau, C.A., Mousas, A., Jiang, T., Chen, M.H., Raffield, L.M., Tardaguila, M., Huffman, J.E., et al. (2020). The Polygenic and Monogenic Basis of Blood Traits and Diseases. Cell *182*, 1214–1231.e11. https://doi.org/10.1016/j.cell.2020.08.008.
61. Auton, A., Abecasis, G.R., Altshuler, D.M., Co-Chair, Durbin, R.M., Co-Chair, Abecasis, G.R., Bentley, D.R., Chakravarti, A., Clark, A.G., Donnelly, P., Eichler, E.E., et al. (2015). A global reference for human genetic variation. Nature *526*, 68–74. https://doi.org/10.1038/nature15393.
62. Chang, C.C., Chow, C.C., Tellier, L.C., Vattikuti, S., Purcell, S.M., and Lee, J.J. (2015). Second-generation PLINK: rising to the challenge of larger and richer datasets. GigaScience *4*, 7. https://doi.org/10.1186/s13742-015-0047-8.
63. Hemani, G., Zheng, J., Elsworth, B., Wade, K.H., Haberland, V., Baird, D., Laurin, C., Burgess, S., Bowden, J., Langdon, R., et al. (2018). The MR-Base platform supports systematic causal inference across the human phenome. eLife *7*, e34408. https://doi.org/10.7554/eLife.34408.
64. Hemani, G., Tilling, K., and Davey Smith, G. (2017). Orienting the causal relationship between imprecisely measured traits using GWAS summary data. PLoS Genet. *13*, e1007081. https://doi.org/10.1371/journal.pgen.1007081.
65. Burgess, S., Dudbridge, F., and Thompson, S.G. (2016). Combining information on multiple instrumental variables in Mendelian randomization: comparison of allele score and summarized data methods. Stat. Med. *35*, 1880–1906. https://doi.org/10.1002/sim.6835.
66. Bowden, J., Davey Smith, G., and Burgess, S. (2015). Mendelian randomization with invalid instruments: effect estimation and bias detection through Egger regression. Int. J. Epidemiol. *44*, 512–525. https://doi.org/10.1093/ije/dyv080.
67. Yavorska, O.O., and Burgess, S. (2017). MendelianRandomization: an R package for performing Mendelian randomization analyses using summarized data. Int. J. Epidemiol. *46*, 1734–1739. https://doi.org/10.1093/ije/dyx034.
68. Tan, Y., Kempchen, T.N., Becker, M., Haist, M., Feyaerts, D., Liu, J., Toma, M., Xiao, Y., Su, G., Rech, A.J., et al. (2025). SPACEc: a streamlined, interactive Python workflow for multiplexed image processing and analysis. Nat. Commun. *16*, 10652. https://doi.org/10.1038/s41467-025-65658-3.
69. Dominguez Mantes, A., Herrera, A., Khven, I., Schlaeppi, A., Kyriacou, E., Tsissios, G., Skoufa, E., Santangeli, L., Buglakova, E., Durmus, E.B., et al. (2025). Spotiflow: accurate and efficient spot detection for fluorescence microscopy with deep stereographic flow regression. Nat. Methods *22*, 1495–1504. https://doi.org/10.1038/s41592-025-02662-x.
70. Virtanen, P., Gommers, R., Oliphant, T.E., Haberland, M., Reddy, T., Cournapeau, D., Burovski, E., Peterson, P., Weckesser, W., Bright, J., et al. (2020). Author Correction: SciPy 1.0: fundamental algorithms for scientific computing in Python. Nat. Methods *17*, 352. https://doi.org/10.1038/s41592-020-0772-5.

Please cite this article in press as: Sloan et al., A sex-specific platelet switch controls anti-tumor immunity in glioblastoma, Cancer Cell (2026), https://doi.org/10.1016/j.ccell.2026.10.004

CellPress
OPEN ACCESS

STAR★METHODS

KEY RESOURCES TABLE

REAGENT or RESOURCE	SOURCE	IDENTIFIER
Antibodies		
CD11b	BD Biosciences	Cat #: 563553; RRID: AB_2738276 Clone: M1/70
CD69	BD Biosciences	Cat #: 741234; RRID: AB_2870786 Clone: H1.2F3
CD11c	BD Biosciences	Cat #: 612796; RRID: AB_2870123 Clone: HL3
CTLA4	BioLegend	Cat #: 106312; RRID: AB_2562340 Clone: UC10-4B9
Ly6G	BD Biosciences	Cat #: 560603; RRID: AB_1727564 Clone: 1A8
PD1	BioLegend	Cat #: 135241; RRID: AB_2715761 Clone: 29F.1A12
CD45R/B220	BioLegend	Cat #: 103237; RRID: AB_10900264 Clone: RA3-6B2
Ki67	BioLegend	Cat #: 652413; RRID: AB_2562664 Clone: 16A8
TIM3	BioLegend	Cat #: 119727; RRID: AB_2716208
CD3	BD Biosciences	Cat #: 564379; RRID: AB_2738780 Clone: 145-2C11
CD45	BD Biosciences	Cat #: 561868; RRID: AB_10893599 Clone: 30-F11
Foxp3	Invitrogen	Cat #: 12-5773-82; RRID: AB_465936 Clone: FJK-16s
LAG3	BioLegend	Cat #: 125224; RRID: AB_2572082 Clone: C9B7W
NK1.1	BioLegend	Cat #: 108716; RRID: AB_493590 Clone: PK136
CD4	BioLegend	Cat #: 100422; RRID: AB_312707 Clone: GK1.5
CD8	BioLegend	Cat #: 100712; RRID: AB_312751 Clone: 53-6.7
CD206	BioLegend	Cat #: 141712; RRID: AB_10900420 Clone: C068C2
Ly6C	BioLegend	Cat #: 128024; RRID: AB_10643270 Clone: HK1.4
CD68	BioLegend	Cat #: 137024; RRID: AB_2616813 Clone: FA-11
CD45	BioLegend	Cat #: 103132; RRID: AB_893340 Clone: 30-F11
CD8a	BD Biosciences	Cat #: 553034; RRID: AB_394572 Clone: 53-6.7
CD4	BD Biosciences	Cat #: 560468: RRID: AB_1645271 Clone: RM4-5
Foxp3	eBioscience	Cat #: 53-5773-82; RRID: AB_763537 Clone: FJK-16s
CD44	BD Biosciences	Cat #: 612799; RRID: AB_2870126 Clone: IM7

(*Continued on next page*)

Please cite this article in press as: Sloan et al., A sex-specific platelet switch controls anti-tumor immunity in glioblastoma, Cancer Cell (2026), https://doi.org/10.1016/j.ccell.2026.10.004

Continued

REAGENT or RESOURCE	SOURCE	IDENTIFIER
IFN-γ	BioLegend	Cat #: 505846; RRID: AB_2563980 Clone: XMG1.2
TNFα	BioLegend	Cat #: 506329; RRID: AB_11123912 Clone: MP6-XT22
Granzyme B	BioLegend	Cat #: 396414; RRID: AB_2810603 Clone: QA18A28
iNOS	Life Technologies	Cat #: 366-5920-82; RRID: AB_2942130 Clone: CXNFT
CD86	BD Biosciences	Cat #: 741946; RRID: AB_2871258 Clone: GL1
CD38	BioLegend	Cat #: 102732; RRID: AB_2734153 Clone: 90
Ly6C	BioLegend	Cat #: 128024; RRID: AB_10643270 Clone: HK1.4
MHCII	BioLegend	Cat #: 107636; RRID: AB_2734168 Clone: M5/114.15.2
B220	BioLegend	Cat #: 103237; RRID: AB_10900264 Clone: RA3-6B2
CD68	BioLegend	Cat #: 137021; RRID: AB_2616811 Clone: FA-11
PD-L1	BioLegend	Cat #: 124319; RRID: AB_2563619 Clone: 10F.9G2
CD8a	BD Biosciences	Cat#: 569278, RRID: AB_3684931; Clone 53-6.7
Ki-67	BioLegend	Cat #: 652428; RRID: AB_2632696 Clone: 16A8
NK1.1	BioLegend	Cat #: 108737; RRID: AB_2562216 Clone: PK136
EGR2	eBioscience	Cat #: 17-6691-80; RRID: AB_11150966 Clone: erongr2
CD206	BioLegend	Cat #: 141712; RRID: AB_10900420 Clone: C068C2
c-Caspase 3	Cell Signaling Technology	Cat #: 94530; RRID: AB_3076239 Clone: 5A1E
c-KIT	Abcam	Cat #: ab32363; RRID: AB_731513 Clone: YR145
CCR7	Abcam	Cat #: ab253187; RRID: AB_2922673 Clone: EPR23192-57
CD11b	Akoya Biosciences	Clone: AKYP0149
CD11c	Akoya Biosciences	Clone: AKYP0130
CD163	Abcam	Cat #: ab182422; RRID: AB_2753196 Clone: EPR19518
CD20	Akoya Biosciences	Clone:AKYP0129
CD206	Akoya Biosciences	Clone: AKYP0137
CD278 (ICOS)	Akoya Biosciences	Clone: AKYP0090
CD304	Abcam	Cat #: ab81321; RRID:AB_1640739 Clone: EPR3113
CD31	Akoya Biosciences	Clone: AKYP0131
CD36	Akoya Biosciences	Clone: AKYP0134
CD39	Akoya Biosciences	Clone: AKYP0107
CD3e	Akoya Biosciences	Clone: AKYP0128
CD4	Akoya Biosciences	Clone: AKYP0146
CD44	Akoya Biosciences	Clone: AKYP0132

(*Continued on next page*)

Please cite this article in press as: Sloan et al., A sex-specific platelet switch controls anti-tumor immunity in glioblastoma, Cancer Cell (2026), https://doi.org/10.1016/j.ccell.2026.10.004

Continued

REAGENT or RESOURCE	SOURCE	IDENTIFIER
CD45	Akoya Biosciences	Clone: AKYP0143
CD45R/B220	Akoya Biosciences	Clone: AKYP0014
CD61/CD41	emFret Analytics	Cat #: M022; RRID: AB_2832609 Clone: Leo.A1
CD62P	Bioss Inc.	Cat #: bs-0561r
CD68	Akoya Biosciences	Clone: AKYP0142
CD8	Akoya Biosciences	Clone: AKYP0145
Col1A1	Akoya Biosciences	Clone: AKYP0141
COL6A1	Abcam	Cat #: ab182744; RRID: AB_2756460 Clone: EPR17072
CXCR4	Abcam	Cat #: ab124824; RRID: AB_2289892 Clone: UMB2
F4/80	Akoya Biosciences	Clone: AKYP0135
FCRγ	Akoya Biosciences	Clone: AKYP0138
FOXP3	Akoya Biosciences	Clone: AKYP0133
Histone H3	Akoya Biosciences	Clone: AKYP0060
Iba1	Akoya Biosciences	Clone: AKYP0140
iNOS	Akoya Biosciences	Clone: AKYP0104
Ki67	Akoya Biosciences	Clone: AKYP0052
Ly6g	Akoya Biosciences	Clone: AKYP0136
MMP9	Abcam	Cat #: ab283575; RRID: AB_2928971 Clone: RM1020
P2RY12	Abcam	Cat #: ab300140 Clone: EPR26298-93
PCNA	Akoya Biosciences	Clone: AKYP0085
PDGFRB	Abcam	Cat #: ab32570; RRID: AB_777165 Clone: Y92
S100A10	Abcam	Cat #: ab76472; RRID: AB_1524359 Clone: EPR3317
S100A9	Akoya Biosciences	Clone: AKYP0144
SMA	Akoya Biosciences	Clone: AKYP0081
SOX2	Akoya Biosciences	Clone: AKYP0106
TCF-1	Akoya Biosciences	Clone: AKYP0099
Ter119	Akoya Biosciences	Clone: AKYP0013
TOX	Akoya Biosciences	Clone: AKYP0098
VCAN	Abcam	Cat #: ab177480; RRID: AB_2827732 Clone: EPR12277
Vimentin	Akoya Biosciences	Clone: AKYP0139
BD Pharmingen™ FITC Rat Anti-Mouse CD62P	BD Biosciences	Cat #: 553744; RRID: AB_395026 Clone: RB40.34
Anti-GP1bα	Emfret analytics	Cat #: R300; RRID: AB_2532218
Anti-mouse CD8α	BioCell	Cat #: BE0061; RRID: AB_1125541 Clone: 2.43
Anti-PAR4 (F2RL3) (extracellular)-FITC Antibody	Alomone Labs	Cat #: APR-034-F; RRID: AB_2040087
PAR4 – 5F10	Marvin Nieman[47]	N/A
SRC (TY418)	Thermo Fisher	Cat #: 14-9034-82; RRID: AB_2572916
SRC	Cell Signaling Technology	Cat #: 2108; RRID: AB_331137
PYK2 (Tyr881)	Thermo Fisher	Cat #: 44-620G; RRID: AB_2533698
PYK2	Cell Signaling Technology	Cat #: 3292; RRID: AB_2174097
Anti-Human CD62P (P-Selectin)	Invitrogen	Cat #: 12-0628-42; RRID: AB_10804401 Clone: AK-4

(*Continued on next page*)

Please cite this article in press as: Sloan et al., A sex-specific platelet switch controls anti-tumor immunity in glioblastoma, Cancer Cell (2026), https://doi.org/10.1016/j.ccell.2026.10.004

Continued

REAGENT or RESOURCE	SOURCE	IDENTIFIER
Biological samples		
Human GBM blood Samples	Cleveland Clinic Rose Ella Burkhardt Brain Tumor and Neuro-Oncology Center Tissue Bank (2559)	N/A
Human Healthy control blood samples	Cleveland Clinic Research Healthy Volunteers biobank (20–413)	N/A
Human GBM patient Tissue	Cleveland Clinic Rose Ella Burkhardt Brain Tumor and Neuro-Oncology Center Tissue Bank (2559)	N/A
Chemicals, peptides, and recombinant proteins		
Thrombin (Human)	Cayman Chemical Company	Cat #: CAYM 13188-250
AY-NH2	Fisher Scientific	Cat #: 1487/1
U46619 (TXA2 Receptor Agonist)	Caymen Chemicals	Cat #: 16450
2-Methylthioadenosine diphosphate trisodium salt	Fisher Scientific	Cat #: 16-241-0
Critical commercial assays		
Thrombin-antithrombin ELISA (TAT)	Abcam	Cat #: ab108907
GPCR Signaling To MAPK/ERK Phospho Antibody Array	Full Moon Biosytems	Cat #: PGP193
Platelet Factor 4 ELISA	Abcam	Cat #: ab202403
Deposited data		
Raw Mouse Platelet Proteomics	This paper	https://doi.org/10.25345/C5VH5CZ89
GPCR Phophoarray Raw Data	This paper	Data S1
Single Cell analysis	This paper	https://zenodo.org/records/21842910
Univariate Cox proportional hazards models	This Paper	https://github.com/andrewdhawan/par4-analysis-scripts
Mendelian Analysis	This Paper	https://github.com/danielrosoff-ui/PAR4-GBM-MR
TCGA Glioblastoma Multiforme (TCGA-GBM)	The Cancer Genome Atlas Research Network	GDC Project ID: TCGA-GBM
CGGA mRNAseq_325	Chinese Glioma Genome Atlas	Dataset: CGGA mRNAseq_325
CGGA mRNAseq_693	Chinese Glioma Genome Atlas	BioProject: PRJCA001747
Glioma International Case-Control Study (GICC)	dbGaP	phs001319
San Francisco Adult Glioma Study (SFAGS-GWAS)	dbGaP	phs001497.v2.p1
National Cancer Institute GliomaScan Study	dbGaP	phs000652
MD Anderson Glioma GWAS (MDA-GWAS)	Ostrom et al.[45]; Melin et al.[46]	Publication-derived cohort
PBMCs from a Healthy Donor: Whole Transcriptome Analysis	10× Genomics	Dataset: pbmcsca
PBMCs from C57BL/6 mice (v1)	10× Genomics	Dataset: pbmcs_1k_v1_mouse
Experimental models: Cell lines		
SB28	Dr. Hideho Okada (University of California San Francisco)	N/A
GL261	Developmental Therapeutics Program, NCI	RRID: CVCL_Y003
KR158	Dr. Loic P. Deleyrolle (Mayo Clinic, previously University of Florida)	N/A
MEG-01	ATCC	Cat #: CRL-2021; RRID: CVCL_0424
Human Brain Microvascular Endothelial Cells	ScienCell	Cat #: 1000; RRID: CVCL_0E09

(*Continued on next page*)

Please cite this article in press as: Sloan et al., A sex-specific platelet switch controls anti-tumor immunity in glioblastoma, Cancer Cell (2026), https://doi.org/10.1016/j.ccell.2026.10.004

Continued

REAGENT or RESOURCE	SOURCE	IDENTIFIER
Experimental models: Organisms/strains		
PAR4$^{-/-}$ C57BL/6	Marvin Nieman (Case Western Reserve University School of Medicine)	N/A
PAR4-P322L C57BL/6	Marvin Nieman (Case Western Reserve University School of Medicine)[23]	N/A
B6.129P2-*Esr2*^{tm1Unc}/J	The Jackson Laboratory	Strain #: 004745; RRID: IMSR_JAX:004745
B6.Cg-435 Tg(Sry)2Ei Srydl1Rlb/JtuJ	The Jackson Laboratory	Strain #: 039108; RRID: IMSR_JAX:039108
NOD.Cg-Prkdcscid Il2rgtm1Wjl/SzJ	The Jackson Laboratory	Strain #: 005557; RRID: IMSR_JAX:005557
B6.129S7-Rag1tm1Mom/J	The Jackson Laboratory	Strain #: 002216; RRID: IMSR_JAX:002216
C57BL/6j	The Jackson Laboratory	Strain #: 000664; RRID: IMSR_JAX:000664
B6.129(Cg)-Foxp3tm3(HBEGF/GFP)Ayr/J	The Jackson Laboratory	Strain #: 016958; RRID: IMSR_JAX:016958
Oligonucleotides		
F2RL3 Forward Primer – Forward AGAAGAGGAGAG-GACACAGAGACAC	Ma et al.[48]	N/A
F2RL3 Forward Primer – Reverse CTTGGCATCGTGGCATCCCTTAG	Ma et al.[48]	N/A
Software and algorithms		
InstanSeg	Goldsborough et al.[49]	[2408.15954] InstanSeg: an embedding-based instance segmentation algorithm optimized for accurate, efficient and portable cell segmentation
Nimbus	Rumberger et al.[50]	GitHub - angelolab/Nimbus · GitHub
FLowSOM	Van Gassen et al.[51]	GitHub - saeyslab/FlowSOM: Using self-organizing maps for visualization and interpretation of cytometry data · GitHub RRID: SCR_016899
QuPath (version: 0.4.0)	Bankhead et al.[52]	https://qupath.readthedocs.io/en/0.4/index.html RRID: SCR_018257
GraphPadPrism (version: 10.0.3)	GraphPad Software Inc.	https://www.graphpad.com/updates/prism-900-release-notes RRID: SCR_002798
FlowJo (version: 10.8.2)	FlowJo, LLC	https://www.flowjo.com/
Enrichr		RRID: SCR_001575

EXPERIMENTAL MODEL AND STUDY PARTICIPANT DETAILS

Human subjects

All subjects were recruited by a coordinator not involved in clinical care and were consented onto the following protocols: 20–413 for healthy subjects (Table S3) and 2559 for GBM patients (Table S4). Patients with a GBM diagnosis were recruited at their pre-op appointment and on the day of surgery for clinical validation of the results reported in this study. All sample information such as patient demographics (gender, age, tumor stage, tumor grade and prior treatments) were obtained as de-identified information associated with the study number for each sample. Healthy control subjects were selected using a matching approach to ensure demographic comparability with the patient cohort. Controls were matched on age and sex and were required to have no known history of malignancy, neurological disorders, autoimmune disease, or other conditions that could influence the study outcomes. Matching was performed at a 1:1 ratio whenever possible. All study procedures were conducted in accordance with the Declaration of Helsinki and our approved local institutional review board protocol at the Cleveland Clinic.

Mice

All animal experiments were performed in accordance with Cleveland Clinic IACUC policies and guidelines and approved by the IACUC committee at Cleveland Clinic Research under the IACUC protocol number 3151 or 2849. C57BL/6 (C57BL/6J is IMSR_JAX:000664), *Rag1*$^{-/-}$ (B6.129S7-*Rag1*^{tm1Mom}/J), four-core genotye (FCG) (B6.Cg-Tg(Sry)2Ei *Sry*^{dl1Rlb}/JtuJ), FOXp3-DTR (B6.129(Cg)-Foxp3tm3(HBEGF/GFP)Ayr/J) and NOD.Cg-*Prkdc*^{scid} *Il2rg*^{tm1Wjl}/SzJ (NSG; RRID:IMSR_JAX:005557) mice were

Please cite this article in press as: Sloan et al., A sex-specific platelet switch controls anti-tumor immunity in glioblastoma, Cancer Cell (2026), https://doi.org/10.1016/j.ccell.2026.10.004

purchased from The Jackson Laboratory as required. PAR4-P322L and PAR4$^{-/-}$ mice were a generous gift from Dr. Marvin Nieman at Case Western Reserve University.[23] Estrogen receptor beta knockout (ERβ$^{-/-}$) mice (B6.129P2-*Esr2*^{tm1Unc}/J) were a generous gift from Dr. Wendy Goodman at Case Western Reserve University. All animal experiments in which a drug was compared with a placebo were conducted in a manner blinded to the research conducting the experiment. The sample size for all mouse experiments was determined by power calculations. All animals were monitored twice daily by investigators, trained veterinary technicians, and licensed veterinarians when needed.

Cell models

The syngeneic mouse GBM cell line SB28 was generously gifted by Dr. Hideho Okada (University of California San Francisco), and KR158 was generously gifted by Dr. Loic P. Deleyrolle (Mayo Clinic, previously University of Florida). The GL261 line was from the Developmental Therapeutics Program, NCI. MEG-01 cells were generously gifted by Dr. Scott J. Cameron (Cleveland Clinic Research). Human brain microvascular endothelial cells were obtained from ScienCell (Cat No. 1000) and grown in endothelial cell medium (ECM, Cat. # 1001) as recommended by the vendor. All cell lines were routinely tested for *Mycoplasma* and were preemptively treated with 1:100 MycoRemoval Agent (MP Biomedicals) upon thawing. All cell lines used in these studies were maintained in complete RPMI 1640 (Media Preparation Core, Cleveland Clinic Research) supplemented with 10% FBS (Thermo Fisher Scientific), 1% penicillin/streptomycin (Media Preparation Core, Cleveland Clinic Research). All cell lines were maintained at 37°C and 5% CO_2 in a humidified incubator.

METHOD DETAILS

Intracranial tumor transplantation and treatments

For intracranial tumor implantation, 4- to 7-week-old mice were intracranially injected with 10,000 to 20,000 cells in 10 μL of RPMI-null media, 3 mm caudal to the coronal structure, 1.8 mm lateral to the sagittal suture at a 90° angle with the skull to a depth of 3.0 mm. Animals were monitored daily for neurological symptoms that include lethargy and hunched posture to signfy signs of tumor burden, at which point the animal was at our definition of humane endpoint. In some experiments, male and female mice were treated with 2 mg/kg BMS986120 (MedChemExpress) or vehicle (8% DMSO) via oral gavage, daily, beginning 1–7 days post tumor implantation depending on the tumor latency of the model. In other experiments, to deplete CD8$^+$ T cells, mice were intraperitoneally injected with an anti-CD8 antibody (BioXCell, Cat. #0061) or isotype control antibody (BioXCell, cat. #BE0090). Animals were administered 200 μg of antibody on day −1, followed by 100 μg every 5 days until humane endpoint was reached as previously described.[10] In other experiments, to deplete platelets, anti-GPIbα (EMFRET, Cat. R300) or anti-igG was administered intraperitoneally 1 day post tumor implantation to avoid hemorrhage at a concentration of 1 μg/g. Subsequent administration was performed at a concentration of 0.5 μg/g every 5 days until humane endpoint was reached.

Ovariectomy

For oophorectomy procedures, 4- to 7-week-old female mice were deeply anesthetized, and a longitudinal incision was made 0.5 cm above where the upper border line of the two hind limbs connect with the back. The skin incision was pulled approximately 0.5 cm horizontally to the left or the right to visualize two soft, white, shiny fat masses next to the lower pole of the kidneys. The left and right ovaries of the mouse are found in the respective fat masses and were bi-laterally ovariectomized by cutting each side of the ovary and excising with sterile surgical scissors, which results in little to no bleeding. After the muscle layer was closed with sutures and the skin incision was sutured or stapled, the mice were placed in a heated chamber to recover. Mice in the sham group also underwent a similar procedure as the ovariectomized group, except the ovaries were left intact and only some adipose tissue near the ovaries was removed.

Human platelet isolation and stimulation

Human platelet isolation was conducted as previously described.[53,54] In brief, whole blood was collected from deidentified GBM patients or healthy donors into tubes containing 3.2% sodium citrate (BD Vacutainer) using a 21-gauge butterfly needle to ensure minimal activation during collection. Platelet-rich plasma (PRP) was obtained by centrifuging the collected blood at 200 × g for 15 min at room temperature, carefully avoiding the buffy coat. PRP was then subjected to a second centrifugation at 200 × g for 15 min to further purify the sample. The resulting supernatant was discarded, and the PRP was diluted 1:1 with Tyrodes buffer. Prostaglandin I2 (PGI2, 10 nM final concentration) was added to prevent spontaneous platelet activation during the isolation process. The PRP-Tyrode's mixture was centrifuged at 1,400 × g for 5 min to pellet the platelets, and the supernatant was removed. Washed platelets were resuspended in Tyrode's buffer and diluted 1:10 to achieve a working platelet suspension. Fifty million platelets per mL was used immediately for subsequent activation assays.

For platelet activation, aliquots of 100 μL of the platelet suspension were stimulated with increasing concentrations of agonists inhibiting the PAR1 receptor (TRAP6), the thromboxane receptor (U46619), the P2Y12 receptor (ADP), and PAR4 (AY-NH2). Agonist concentrations ranged from 0.01 μM to 20 μM for TRAP6, U46619, and ADP, and from 0.05 μg/mL to 1 μg/mL for CRP. After a 15-min stimulation at room temperature, 1 μL of P-selectin antibody (anti-CD62P, clone AK-4, eBioscience) conjugated to PE was added to each sample and incubated in the dark for 30 min to prevent photobleaching.

Please cite this article in press as: Sloan et al., A sex-specific platelet switch controls anti-tumor immunity in glioblastoma, Cancer Cell (2026), https://doi.org/10.1016/j.ccell.2026.10.004

Following antibody staining, 100 μL of 2% formalin was added to each sample to fix the platelets. Fixed samples were stored at 4°C for no longer than 16 h prior to analysis. Flow cytometry was performed on a BD Accuri C6, and fluorescence was detected using the FL-2 channel (for PE-conjugated antibodies). Platelet activation was quantified based on the surface expression of CD62P, with data analyzed using FlowJo software.

Mouse platelet isolation and stimulation

Whole blood was collected from C57BL/6 mice via retro-orbital bleeding using heparinized capillary tubes. Blood was drawn into tubes containing heparin/Tyrode's solution (1000 U/mL heparin in Tyrode's buffer, 1:20 dilution). The collected blood was gently mixed by inverting the tube and processed immediately. PRP was isolated by centrifuging the whole blood at 1000 RPM for 5 min at room temperature. Plasma was carefully collected, avoiding red blood cells, and subjected to a second centrifugation at 1000 RPM for 5 min to remove remaining blood cells. The PRP was then supplemented with 1 μM PGI2 to prevent platelet activation during isolation. The platelet pellet was obtained by centrifuging PRP at 2700 RPM for 5 min, after which the supernatant was discarded. Platelets were resuspended in Tyrode's buffer and pooled to achieve a final concentration suitable for stimulation experiments. Platelets were aliquoted into 96-well plates at a concentration of 100 μL per well for subsequent activation assays.

For platelet activation, 1 μL of each agonist (thrombin, U46619, ADP, convulxin) was added to the platelets, with final concentrations ranging from 0.1 to 20 μM, depending on the agonist. Platelet stimulation was carried out at room temperature for 10 min. After stimulation, 1 μL of FITC-conjugated anti-CD62P antibody (clone RB40.34, BD Biosciences) was added to each sample, and the platelets were incubated in the dark for an additional 10 min to prevent photobleaching.

Following staining, 100 μL of 2% formalin was added to fix the platelets, and samples were either immediately analyzed by flow cytometry or stored at 4°C for up to 16 h prior to analysis. Flow cytometry was performed on a BD Accuri C6 cytometer, and data were collected for 10,000 events per sample. The expression of P-selectin (CD62P) on the platelet surface was used as an indicator of platelet activation, and data analysis was carried out using FlowJo software.

Platelet light transmission aggregometry

To determine whether long-term treatment with BMS986120 affected platelet aggregation *ex vivo*, blood was collected from vehicle- and BMS986120-treated male and female mice, and platelets were isolated as described above. Platelet-depleted plasma (PDP) was prepared from the remaining blood samples by centrifugation at 2,500 × g for 10 min and was used to establish the baseline optical density. Platelet counts were adjusted to 8×10^6 platelets/mL in platelet-rich plasma (PRP) using PDP. Platelet aggregation was assessed following stimulation with thrombin (1 Units/mL). Aggregation responses were compared between treatment groups and between male and female mice.

Immunophenotyping by flow cytometry

At the designated time points, tumor-bearing left hemispheres were enzymatically digested using collagenase IV (Sigma) and DNase I (Sigma) to generate a single-cell suspension, subjected to a Percoll centrifugation step, and then filtered through a 40-μm strainer. Cells were first stained with LIVE/DEAD Fixable Stains (Thermo Fisher) on ice for 15 min, washed with PBS, and resuspended in an Fc receptor blocker (Miltenyi Biotec) diluted in PBS/2% BSA, followed by incubation on ice for 10 min. Surface staining was performed using fluorochrome-conjugated antibodies diluted in brilliant buffer (BD Biosciences) at a concentration of 1:100 to 1:250, with a 30-min incubation on ice. After a subsequent wash in PBS/2% BSA, cells were fixed overnight using Foxp3/Transcription Factor Fixation Buffer (eBioscience).

For intracellular staining, antibodies were prepared in permeabilization buffer at 1:250 to 1:500 and incubated at room temperature for 45 min. To detect intracellular cytokines, cells were stimulated in complete RPMI medium using a Cell Stimulation Cocktail with a protein transport inhibitor (eBioscience) for 4 h. Following stimulation, cells underwent the same staining procedures as described above.

In vitro $CD8^+$ T cell culture

$CD8^+$ T cells were extracted from the splenocytes of C57BL/6 mice using a magnetic bead isolation kit (STEMCELL Technologies), following established protocols. The cells were then maintained in complete RPMI medium supplemented with recombinant human IL-2 (30 U/mL, PeproTech) and activated using anti-CD3/anti-CD28 Dynabeads (Invitrogen) at a bead-to-cell ratio of 1:10. In addition, platelets were isolated as previously described and incorporated into the T cell culture for three consecutive days at a 1:1 ratio of $CD8^+$ T cells to platelets. Cells subsequently underwent the same staining procedures outlined above.

MEG-01 cell culture experiments

MEG-01 cells were cultured in RPMI compete media as described above and treated with β-estradiol (0, 0.01, 0.1, 1.0, and 10 μg/mL), dihydrotestosterone (0, 0.01, 0.1, 1.0, and 10 μg/mL), and progesterone (0, 0.01, 0.1, 1.0, and 10 μg/mL) for 4 consecutive days for quantitative real-time PCR (qPCR), immunoblotting and GPCR phospho antibody array (Full Moon Biosystems).

Immunoblotting, antibodies, and GPCR phospho antibody array

Lysates were prepared as previously described by our group.[4,55] Cells were washed with PBS and lysed in NP-40 lysis buffer (0.5% NP-40, 10 mM Tris-Cl pH 7.5, 1 mM EDTA pH 8.0, 150 mM NaCl) supplemented with 1% protease and phosphatase inhibitors

Please cite this article in press as: Sloan et al., A sex-specific platelet switch controls anti-tumor immunity in glioblastoma, Cancer Cell (2026), https://doi.org/10.1016/j.ccell.2026.10.004

(Sigma-Aldrich). Lysates were clarified by centrifugation at 21,000 × g for 10 min at 4°C, and protein concentration was determined using the Bio-Rad protein assay with BSA as the standard.

For immunoblotting, equal amounts of protein (15–50 μg) were resolved by SDS-PAGE on pre-cast 4–15% gels (Bio-Rad) and transferred to PVDF membranes (Millipore). The membrane was subsequently rinsed in Tris-buffered saline (TBS; 50 mM Tris-HCl 150 mM NaCl, pH 7.6) and blocked in Intercept blocking buffer for one hour (Li-Cor, 927–50000, Lincoln, NE) prior to the application of primary antibodies targeting Actin (1:1000) (Millipore Sigma, MAB1501PAR4, PAR4 (1:500) (Generated by Marvin Nieman),[47] p-SRC (Tyr418) (1:1000) (ThermoFisher, 14-9034-82), SRC (1:1000) (Cell Signaling 2108), P-PYK2 (Tyr881) (1:1000) (ThermoFisher, 44-620G), and PYK2 (1:1000) (ABCAM, ab32571). The membrane was incubated overnight at 4°C with the primary antibody and rinsed with TBS-T (TBS; 50 mM Tris-HCl 150 mM NaCl, 1% Tween 20 v/v% pH 7.6) followed by incubation in secondary (IRDye 680- and IRDye 800CW-conjugated secondary antibodies, Li-Cor, 926–68072 and 926–32213, respectively) for one hour at room temperature prior to visualization on the Li-Cor Odyssey CLx imaging System (Li-Cor, Lincoln, NE). Western blot analysis of band intensity was completed using Image Studio Analysis software from Li-Cor. Alternatively, membranes were incubated with primary antibodies in 5% BSA in TBST at 4°C for 2–7 days, washed with TBST, and then incubated with HRP-conjugated secondary antibodies for 2.5–3 h at room temperature. Blots were developed using enhanced chemiluminescence (ECL) and imaged on a Bio-Rad ChemiDoc MP system. Actin was used as a loading control.

The GPCR phospho antibody array (Full Moon Biosystems, PGP193) was conducted following the protocol as described by the manufacturer. Following array incubation in antibody, slides were sent to Full Moon Biosystems for analysis, and array signal intensity was quantified as the median signal per spot and averaged across replicate spots for each antibody, with variability assessed by coefficient of variation. Data were normalized to the median signal intensity across the array. Fold changes were calculated as the ratio of treatment to control from normalized values, with increased or decreased expression indicated by red or green shading, respectively. For phospho-arrays, signaling ratios were calculated as the phospho-specific signal divided by the corresponding total protein signal, and fold changes were similarly determined between treatment and control samples.

Co-immunoprecipitation

Co-immunoprecipitations were done as previously described.[56] Briefly, either MEG-01, brain microvascular endothelial cells, or human platelets were lysed on ice for 2 h in 1.0 mL immunoprecipitation (IP) buffer containing 25 mM Tris (pH 7.4), 1 mM $MgCl_2$, 2 mM EDTA, 150 mM NaCl, 1.0% Triton X-100, and Complete Protease Inhibitor Cocktail (Roche). Protein G–Sepharose Fast Flow beads (100 μL; MilliporeSigma) were washed twice with IP buffer (500 × g, 5 min), blocked for 1 h in 5.0% BSA prepared in IP buffer, and resuspended in 1.0 mL IP buffer. Lysates were clarified by centrifugation (12,000 × g, 10 min, 4°C), and 10% of the supernatant (50 μL) was retained as the input control. The remaining lysate was split into two equal aliquots and incubated overnight at 4°C with Protein G beads and either 2 μg of the indicated primary antibody or an isotype-matched IgG control. Following incubation, samples were centrifuged at 500 × g for 5 min, and 50 μL of the supernatant was collected as the unbound fraction. Beads were washed four times with IP wash buffer (25 mM Tris [pH 7.4], 10 mM $MgCl_2$, 2 mM EDTA, 0.1% Triton X-100), with 50 μL aliquots retained after the first and fourth washes. After the final wash, bound proteins were eluted by denaturation in 2× SDS sample buffer and heating at 95°C for 10 min. Samples were resolved by SDS-PAGE and transferred to nitrocellulose membranes as described above.

Quantitative real-time PCR (qPCR)

MEG-01 cell were incubated at 37°C in a humidified incubator with 5% CO_2, then rinsed with HBSS. RNA was isolated using the RNeasy Mini Kit, quantified for quality and concentration, and reverse-transcribed to cDNA. Quantitative PCR was performed using SYBR Green chemistry on an Applied Biosystems QuantStudio 3 system to assess expression Reactions (20 μL) were run in triplicate for 40 cycles, and relative expression was calculated using the ΔΔCT method. Primers used were specific for actin (5′-AGAAAATCTGGCACCACACC-3′, 5′-AGAGGCGTACAGGGATAGCA-3′) and PAR4 (5′-CCGCTGCTGTATCCTTTGGT -3′, 5′-TCC TTGAGTTCTACTGTGGGAC-3′).

MEG-01 calcium imaging

Washed MEG-01 cells were pre-incubated with BMS986120 (10 nM), β-estradiol (0, 0.01, 0.1, 1.0, and 10 μg/mL), dihydrotestosterone (0, 0.01, 0.1, 1.0, and 10 μg/mL), and progesterone (0, 0.01, 0.1, 1.0, and 10 μg/mL). Afterward, washed MEG-01 cells were loaded with Fura-2 AM (5 μM, 1 h at 37°C), pelleted by centrifugation (2700 rpm, 5 min) in the presence of 10 μM PgI_2, and resuspended in fresh Tyrode's solution in a 96-well plate. Intracellular calcium flux was measured over 10 min by ratiometric fluorescence (340/380 nm) following automated addition of thrombin (1.0 Units/mL) using a FlexStation 3 system. Data are presented as normalized fluorescence changes relative to baseline (F/F_0) as previously described.[53]

ELISA

Plasma was isolated from GBM patients or matched healthy control patient blood by centrifuging whole blood at 2000 x g for 10 min. Plasma was isolated, and a human thrombin anti-thrombin was measured using a simple step ELISA kit and the subsequent protocol (ABCAM, ab108907). Platelet Factor 4: Intracranial tumor implantations were conducted as described above. Prior to tumor cell implantation or following tumor formation (14 days post tumor cell implantation for SB28, and 28 days post tumor cell implantation for KR158), whole blood was collected from C57BL/6 mice via retro-orbital bleeding using heparinized capillary tubes. Plasma was isolated from whole blood by centrifuging at 2000 x g for 10 min. Plasma was isolated, and mouse platelet factor 4 expression was measured using a simple step ELISA kit and the subsequent protocol (ABCAM, ab202403). IFNγ: $CD8^+$ T cells were extracted

Please cite this article in press as: Sloan et al., A sex-specific platelet switch controls anti-tumor immunity in glioblastoma, Cancer Cell (2026), https://doi.org/10.1016/j.ccell.2026.10.004

from the splenocytes of C57BL/6 mice using a magnetic bead isolation kit (STEMCELL Technologies) and exposed to platelets at a 1:1 ratio as described above. Following 4 days of platelet – T cell co-incubation, conditioned media was collected by centrifuging the medium cell mixture at 1300 x g for 4 min; conditioned medium was removed and saved for ELISA. Following centrifugation, IFNγ was measured using a simple step ELISA kit and the subsequent protocol (ABCAM, ab100689).

PAR4 immunohistochemistry

Seven formalin-fixed, paraffin-embedded (FFPE) tissue specimens were subjected to standard immunohistochemistry to visualize the PAR4 receptor. Four specimens were obtained from GBM patients (two male, two female; age range 62–74 years) and were isolated from the cerebral cortex of postmortem brain tissue. Antibody recognition and staining were optimized using a sample of human colon of unknown sex and age as a positive control, and cortical specimens from a 64-year-old female and a 74-year-old male with neurodegenerative disease served as negative controls. With the exception of the positive control, all tissue was curated by Dr. Peter LaViolette and his team at the Medical College of Wisconsin. 10 μm sections were prepared and subjected to standard immunohistochemistry protocols. The PAR4 receptor (mouse anti-PAR4, clone 5F10[47]) was visualized using 3,3′-diaminobenzidine (DAB) chromogen, and nuclei were counterstained with hematoxylin.

MEG-01 immunofluorescence

MEG-01 cells were collected by combining cells in suspension with adherent cells detached using Accutase. Cells were centrifuged for 5 min at 500 × g, washed once with PBS, and centrifuged again for 5 min at 500 × g. Cells were fixed in 4% paraformaldehyde (PFA) for 20 min at room temperature, washed twice with PBS, and incubated for 1 h at room temperature in blocking buffer consisting of PBS containing 0.1% Triton X-100 and 5% BSA. Cells were then incubated overnight at 4°C with rabbit anti-PAR4 antibody (Alomone Labs) and mouse anti-ERβ antibody (Invitrogen), each diluted 1:100 in blocking buffer. The following day, cells were centrifuged for 5 min at 500 × g, washed twice with PBS, and incubated for 1 h at room temperature in the dark with Alexa Fluor 488-conjugated goat anti-rabbit IgG and Alexa Fluor 647-conjugated goat anti-mouse IgG secondary antibodies, each diluted 1:100, together with phalloidin-fluor 555 plus (Thermo-Fisher) diluted 1:400 in blocking buffer. Following staining, cells were washed with PBS and mounted onto glass slides using DAPI Fluoromount-G (ThermoFisher). Images were acquired on a Leica TCS SP8 confocal microscope using a 100×/1.40 NA oil immersion objective. Z-stacks were acquired at 0.6 μm intervals across the full cell height. Acquisition parameters were kept constant across samples. For visualization, images were generated using the free Imaris Viewer (Oxford Instruments).

Assembly and testing of human cancer-associated thrombosis tissue microarray

A cohort of 53 patient pathological specimens was collected, comprising 8 specimens with no evidence of thrombus and 45 specimens in which thrombosed blood vessels were clearly evident within the tumor microenvironment. Male and female patients were equally represented, and all specimens were obtained from adult patients. Tumor-associated thrombi were identified by Dr. Gabrielle Yeaney, a Cleveland Clinic staff physician and board-certified neuropathologist. A specimen was classified as non-thrombotic if and only if no blood vessels within the sample contained thrombus; thrombosed specimens presented with at least one occluded vessel within the tissue.

To construct the tissue microarray (TMA), 2-mm circular cores were removed from the original paraffin-embedded tissue specimens and transferred into a multi-core array. For thrombosed specimens, core sites were selected to capture as many thrombotic events as possible.

10 μm sections of the tissue microarray were prepared and subjected to ultra-high-plex sequential immunohistochemistry using the Akoya Biosciences PhenoCycler-Fusion 2.0 platform. A custom-built panel of 76 antibodies was applied to the arrayed tissue samples.

High-resolution images were analyzed using multiple pipelines within QuPath (version 0.7.0), including pixel and object classification, to segment irregularly shaped neural, immune, vascular, and tumor cells. Positive cell detection was used to quantify cell-type abundance. Data were visualized using GraphPad Prism (version 11) or Claude (Anthropic, Claude Opus 5) generative AI.

Mouse platelet proteomics

Sample preparation

To each platelet cell pellet, 600 μL of chilled methanol:water (4:1) was added, and the cells were lysed by sonication for 2 min in a water bath. The samples were incubated at −20°C for 1 h before centrifugation at 10,000 × g for 15 min. The supernatant was removed and the protein pellet was dried in a SpeedVac and solubilized in 150 μL urea buffer (100 mM TrisHCl buffer, 8M urea, 1× protease inhibitor cocktail, pH 8.0). The protein concentrations of the samples wereestimated using a BCA assay, and a 300 μg aliquot of protein from each sample was mixed with 134 μL 100 mM TrisHCl buffer with 1× HALT protease and phosphatase inhibitor mixture. The samples were reduced by dithiothreitol and alkylated by iodoacetamide and precipitated using −20°C acetone overnight. After centrifuging at 15,000 x g for 15 min, acetone was decanted, and the protein pellets were air dried for 30 min in a fume hood. The dried samples were suspended in 300 μL 50 mM triethyl ammonium bicarbonate (TEAB) and digested using 4 μg trypsin per sample. After overnight incubation in 37°C with 500 rpm shaking on a Thermomixer, digested samples were centrifuged at 21,000 x g for 15 min, and a 20 μg aliquot of each sample was removed for global proteomics. The remaining protein was subjected to phosphopeptide enrichment using Hi-Select TiO2 Phosphopeptide Enrichment Kit (ThermoScientific A32993), and the eluted peptides

Please cite this article in press as: Sloan et al., A sex-specific platelet switch controls anti-tumor immunity in glioblastoma, Cancer Cell (2026), https://doi.org/10.1016/j.ccell.2026.10.004

were dried immediately in a SpeedVac. Each sample was reconstituted in 20 μL 0.1% formic acid and was ready for LCMS analysis.

LC-MS/MS: Phosphoproteomics

The phosphoenriched samples were analyzed by LC-MS using a Orbitrap Exploris 480 instrument (ThermoScientific) equipped with a Vanquis *NEO* UHPLC system. The peptide aliquots were injected onto a ThermoScientific PepMap *NEO* C18 (30 μm × 5 mm, 5 μm) trapping column then eluted onto a ThermoScientific Easy Spray Pepmap *NEO* C18 (50 cm × 75 μm id, 2 μm 100 Å) reversed-phase analytical column. Peptides were separated using a 120-min acetonitrile/0.1% formic acid gradient at a flow rate of 0.3 μL/min. These samples were analyzed using a data-dependent-analysis (DDA) to identify the peptides and proteins present in the sample. This experiment involved an initial MS1 scan between 350 and 1400 Da in the orbitrap at a resolution of 120k followed by data dependent MS2 scans (Top 20) using HCD at 30% nCE with Orbitrap detection at a resolution of 15k. Dynamic exclusion was enabled where ions within 10 ppm were excluded for 30 s.

LC-MS/MS: Global proteomics

The proteomics experiments were performed using a Data Independent Acquisition (DIA) strategy. For these experiments, a NanoElute HPLC was coupled to a TimsTof Pro2 Q-Tof mass spectrometry system (Bruker Daltonik GmbH, Bremen). The HPLC was equipped with a Bruker 15 cm × 75 μm id C18 ReproSil AQ, 1.9 μm, 120 Å reversed-phase capillary chromatography column. Peptide separation was performed using a 50 min gradient from 2 to 35% mobile phase B, where mobile phase A was 0.1% formic acid and mobile phase B was acetonitrile/0.1% formic acid at a flow rate of 0.3 μL/min.

To build a spectral library, 5 μg from each of the digested samples were pooled. The pooled sample was desalted using a Waters C18 Sep-Pak cartridge. The desalted pooled sample was offline fractionated into 16 fractions using a high pH reversed phase HPLC method on a Waters XBridge BEH C18 2.1 mm × 150 mm, 3.5 μm, 130 Å chromatographic column using a 48-min from 2 to 90% mobile phase B, where mobile phase A was 0.1% formic acid 10 mM ammonium formate in water and mobile phase B was 90% acetonitrile/0.1% formic acid 10 mM ammonium formate in water at a flow rate of 0.25 mL/min. Fractions were dried in a SpeedVac and reconstituted in 50 μL 0.1% formic acid each. Ten microliters from each fraction was mixed with 10 μL 0.5× concentration iRT standards, and the samples were ready for LCMS analysis. For spectral library generation, the fractionated samples were analyzed using a Parallel Accumulation–Serial Fragmentation (PASEF) data-dependent acquisition (DDA) method. This method utilized MS1 scans for the identification of precursor ions followed by 10 PASEF MS/MS scans. The tims-MS survey scan was acquired between 0.60 and 1.43 Vs/cm2 and 100–1,700 m/z with a ramp time of 100 ms. The total cycle time for the PASEF scans was 1.17 s, and the MS/MS experiments were performed with collision energies between 20 eV (0.6 Vs/cm2) and 59 eV (1.6 Vs/cm2). Precursors with 2–5 charges were selected with the target value set to 20,000 a.u and intensity threshold to 2,500 a.u. Precursors were dynamically excluded for 0.4 min.

For protein quantitation, each sample was analyzed using a PASEF DIA method, which includes an MS1 full scan followed by MS/MS scans of 32 fixed mass windows between 400 m/z and 1201 m/z. The TIMS-MS survey scan was acquired between 0.60 and 1.43 Vs/cm2 and 100–1,700 m/z with a ramp time of 100 ms. The total cycle time for the PASEF scans was 1.8 s and the MS/MS experiments were performed with collision energies between 20 eV (0.85 Vs/cm2) and 59 eV (1.3 Vs/cm2).

Data analysis: Phosphoproteomics

The LC-MS/MS data were searched against the mouse SwissProtKB database downloaded on 3-23-2022 (17.552 entries) using the program Proteome Discoverer 2.5. These searches were performed considering full tryptic peptides with no more than 3 missed cleavage sites. The MS1 and MS2 mass accuracies were set to 10 ppm and 0.06 Da, respectively;carbamidomethylation was considered as a fixed modification; and oxidation of methionine, phosphorylation at S,T, and Y residues, and protein acetylation were considered as variable modifications. The results were filtered using a reverse decoy database strategy with peptide FDR rates of 1%. LFQ analysis was performed using the Minora Feature Detector node, and the LC-MS data was normalized to total peptide abundance.

Label-free quantitation was performed using the Minora Feature Detector Node bundled into PD2.5 algorithm. Quantitation was performed on unique peptides, and only proteins identified by two peptides and the LFQ intensities were normalized to total peptide content for each LC-MS experiment. The LFQ intensities were used to determine the abundance ratios of the protein across groups, and significance was determined using a *t* test derived *p*-value.

DIA data analysis

The spectral library was generated using Pulsar integrated in Spectronaut V16 to search the DDA LC-MS data against the mouse SwissProt protein sequence database (Downloaded 2.24.2026 with 17,137 Entries). Oxidation of Met and protein N-terminal acetylation were set as variable modifications, and carbamidomethylation of Cys was set as fixed modification. The false discovery rate (FDR) of protein, peptide, and peptide spectral match (PSM) were all set to 1% of the identifications from a decoy database generated by reversing the amino acid sequences of the mouse SwissProt protein database. The iRT Reference Strategy was set to Deep learning assisted iRT regression. The DIA data of the samples were searched using Spectronaut V19 software against the spectral library and the mouse SwissProt protein sequence database. The relative abundance of the proteins in these samples was determined using a label free quantitation (LFQ) approach. Protein quantities were expressed as normalized intensities by Spectronaut V17. These are based on the sum of the (raw) intensities of the MS/MS product ions of their peptide precursor peaks that are normalized on total peptide quantities of each sample to ensure that profiles of the abundances across samples accurately reflect the relative amounts of the proteins.

Please cite this article in press as: Sloan et al., A sex-specific platelet switch controls anti-tumor immunity in glioblastoma, Cancer Cell (2026), https://doi.org/10.1016/j.ccell.2026.10.004

Platelet gene signature analysis

Gene set enrichment analysis

Gene set enrichment analysis was performed using the Enrichr web-based platform to identify biological pathways and functional annotations associated with platelet-expressed genes as previously reported.[57] Gene lists derived from mouse platelet datasets were submitted to Enrichr and queried against curated gene set libraries. Enrichment significance was calculated using the Enrichr combined score, which integrates the enrichment *p*-value obtained from Fisher's exact test with the deviation from the expected rank (*Z* score). Significantly enriched pathways and biological processes were identified based on adjusted *p*-values and combined enrichment scores.

Univariate Cox proportional hazards analysis

Patient samples and datasets

This study utilized WHO grade 4 IDH wild-type GBM samples from four publicly available datasets: The Cancer Genome Atlas (TCGA), Chinese Glioma Genome Atlas (CGGA_325, CGGA_893), and Glioma Longitudinal Analysis (GLASS).

Immune cell profiling

The relative abundance of 22 immune cell subtypes within each tumor sample from each dataset was estimated using CIBERSORTx with default parameters and the LM22 signature gene set. Additionally, a gene signature for platelet expression (REACTOME_RESPONSE_TO_ELEVATED_PLATELET_CYTOSOLIC_CA2, MSigDB) was scored for each sample using single sample gene set enrichment analysis (ssGSEA).

Univariate survival analysis

To evaluate the prognostic significance of immune cell infiltration, univariate Cox proportional hazards models were constructed for each estimated immune cell population (including the Platelet Sig score) within each dataset. Immune cell proportions and platelet signature score were *Z* score normalized and centered prior to hazard ratio computation. Immune cell abundance and platelet signature score (platelet_sig) were dichotomized at the median value for each cell type within each respective dataset. The resulting hazard ratios (HRs) for overall survival are presented, with error bars indicating the 95% confidence intervals.

Immune cell correlation analysis

Spearman correlation coefficients between the estimated abundances of the major immune cell types and platelet gene signature score were computed. Correlation coefficients were computed for each of the major immune cell subtypes (B cells, dendritic cells (DCs), T cells, NK cells, mast cells, microglia, monocytes, and macrophages) within each dataset (CGGA_325, GLASS, TCGA).

Analysis of previously published scRNA-seq data

Publicly available single-cell RNA sequencing (scRNA-seq) count matrices from healthy human peripheral blood mononuclear cells (PBMCs) and C57BL/6 mouse PBMCs were obtained from the 10× Genomics data repository. Raw gene expression matrices were imported into R and analyzed using the Seurat package (v4.3.0) for quality control, normalization, identification of highly variable features, and data scaling. Principal component analysis (PCA) was performed for dimensionality reduction, followed by Uniform Manifold Approximation and Projection (UMAP) for visualization of cellular heterogeneity and cluster relationships.[58]

To facilitate cell-type annotation, integrated Seurat objects were uploaded to BioTuring Browser, which utilizes deep learning-based reference mapping and cell identity prediction algorithms. Predicted cell identities were subsequently validated through manual inspection of canonical lineage-specific marker genes. Data visualization and figure generation were performed in R using functions from the ggplot2 and scCustomize packages.

To investigate the expression profile of PAR4 (*F2RL3*) across distinct cell populations within the glioblastoma tumor microenvironment (TME), we analyzed single-cell RNA sequencing data from the GBMap dataset.[59] Cell-type annotations were based on previously established classifications within the dataset. Expression of *F2RL3* was quantified across annotated cellular subsets, and results were visualized using a Seurat-generated dot plot (v5), where dot size represents the proportion of expressing cells and color intensity reflects normalized expression levels.[58]

Mendelian randomization analysis

We used two-sample, *cis*-restricted (drug-target) Mendelian randomization (MR) to test whether genetically proxied perturbation of platelet-pathway drug targets is associated with GBM risk. Genetic variants (G) serve as instrumental variables (IVs) for the effect of an exposure (X; platelet count) on an outcome (Y; GBM risk) under three assumptions: IV1 (relevance), the instruments are robustly associated with the exposure; IV2 (independence), the instruments are independent of confounders (U) of the exposure–outcome relationship; and IV3 (exclusion restriction), the instruments affect the outcome only through the exposure (Figure S3A). All analyses used European-ancestry summary statistics on genome build GRCh37/hg19.

Data sources

The exposure was platelet count from Vuckovic et al.,[60] obtained from the NHGRI–EBI GWAS Catalog under accession GCST90002402 (*N* = 408,112, European ancestry). The outcome was GBM risk from the age-stratified GBM GWAS meta-analysis of Ostrom et al.,[45] which combined four European-ancestry glioma GWAS — the Glioma International Case-Control Study (GICC), the San Francisco Adult Glioma Study (SFAGS-GWAS), the MD Anderson Glioma GWAS (MDA-GWAS) and the National Cancer Institute GliomaScan study — comprising 4,512 GBM cases and 10,582 controls (62.8% of cases male; mean age at diagnosis 57.5 years). GBM cases were divided into tertiles of the case age-at-diagnosis distribution (18–53, 54–63 and 64+ years), and

Please cite this article in press as: Sloan et al., A sex-specific platelet switch controls anti-tumor immunity in glioblastoma, Cancer Cell (2026), https://doi.org/10.1016/j.ccell.2026.10.004

each age stratum was compared against the full control set using age-stratified logistic regression adjusted for sex and study-specific principal components, with study-level results combined by inverse-variance-weighted fixed-effect meta-analysis. Because the three strata share a common control set, the stratum-specific estimates are not statistically independent. Linkage disequilibrium (LD) was estimated from the 1000 Genomes Phase 3 European reference panel (GRCh37).[61]

Instrument selection and clumping

For each of five platelet-pathway targets — *F2*, *F2R* (PAR1), *F2RL3* (PAR4), *TBXA2R* (TBXA2), and *P2RY12* (P2Y12) — we retained exposure variants lying within ±500 kb of the gene body (Ensembl GRCh37 coordinates) and associated with platelet count at $p < 5 \times 10^{-6}$ (primary threshold; $p < 5 \times 10^{-8}$ and $p < 5 \times 10^{-4}$ were examined as sensitivity analyses). Because correlated-instrument MR gains power by retaining partially correlated cis variants, instruments were clumped at $r2 < 0.2$ within a 10,000 kb window (rather than the conventional $r2 < 0.001$) using PLINK v1.9 4 against the 1000 Genomes Phase 3 EUR panel.[62]

Harmonization

Outcome variant identifiers were standardized to rsIDs against the 1000 Genomes Phase 3 EUR reference (matched on rsID where present, otherwise on chromosome and position), and per-allele odds ratios were converted to the log-odds scale ($\beta = \log[OR]$). Exposure and outcome were harmonized assuming forward-strand alleles (TwoSampleMR harmonise_data, action = 1)[63]; Steiger filtering was applied to exclude variants explaining more variance in the outcome than in the exposure[64]; and exposure and outcome effect estimates were aligned to the reference allele of the LD correlation matrix prior to analysis.

Estimators and sensitivity analyses

The primary estimator was inverse variance weighted (IVW) MR accounting for the LD correlation matrix among instruments.[65] Sensitivity analyses comprised correlated MR-Egger (fitted where ≥3 instruments were available, with the intercept used as a test of directional horizontal pleiotropy) and correlated maximum-likelihood MR; where[66] a single instrument was retained (P2RY12), the Wald ratio was used. Robustness was further assessed across the three-instrument *p*-value thresholds and across the three age-at-onset strata. Estimates are reported as odds ratios for GBM with 95% confidence intervals per one standard-deviation change in genetically proxied platelet count at each target locus (Figures S3B and S3C).

Software

Analyses were performed in R v4.5.1 using TwoSampleMR v0.6.18,[63] MendelianRandomization v0.10.0 9,[67] ieugwasr v1.1.0, genetics.binaRies v0.1.2, data.table and dplyr, with PLINK v1.90b6.21.[62] Analysis code is available at https://github.com/danielrosoff-ui/PAR4-GBM-MR.

Akoya multispectral immunofluorescence

PhenoCycler-fusion slide preparation

FFPE tissue slides were baked at 60°C overnight. Baked slides were deparaffinized with Xylene Substitute solution (Epredia) and rehydrated in a series of gradient ethanol solutions, ranging from 100% to ddH2O. The slides were then placed in a glass Coplin jar containing 1× antigen retrieval buffer (pH 9.0) (Akoya Biosciences), and antigen retrieval was performed with an Instant Pot using the high-pressure setting for 20 min. Following antigen retrieval, the slides were cooled in the retrieval buffer to room temperature and transferred to a transparent slide container with an autofluorescence bleaching solution (4.5% w/v H2O2 and 20mM NaOH in PBS). The container was sandwiched between two LED lamps, and the slides were photobleached for 90 min at RT, with fresh bleaching solution replenished once after 45 min. Slides were then processed according to the PhenoCycler-Fusion User Guide (PD-000011 Rev S, Akoya Biosciences). Briefly, slides were washed in Hydration Buffer, equilibrated in Staining Buffer, and incubated overnight at 4°C with a 47-marker antibody cocktail (Table S8) prepared in Blocking Buffer. The slides were then washed in Staining Buffer, gently fixed with 1.6% formaldehyde, washed in PBS, and incubated in ice-cold methanol for 5 min. The slides were then washed in PBS, fixed with Final Fixative Solution for 20 min, washed in PBS, and preserved in Storage Buffer at 4°C before the PCF run.

PhenoCycler-fusion setup and data acquisition

The experimental protocol was set up using the PhenoCycler Experiment Designer (Version 2.2.0). A reporter plate containing fluorescently labeled reporters was prepared according to the PhenoCycler-Fusion User Guide (PD-000011 Rev S, Akoya Biosciences). Slides were prepared for the PCF instrument according to the PhenoImager Fusion 2.0 User Guide (PD-000088 Rev G, Akoya Biosciences). Briefly, slides were removed from the Storage Buffer and incubated in PBS for 10 min at room temperature. After incubation, a Flow Cell (Akoya Biosciences) was attached to each sample slide using the Flow Cell Assembly Device (Akoya Biosciences). The slide with the attached Flow Cell (Sample Flow Cell) was equilibrated in 1× PCF buffer for 10 min at RT. PhenoCycler-Fusion software (Version 2.4.0) was used to set up the imaging run on the PCF instrument according to the PhenoImager Fusion 2.0 User Guide (PD-000088 Rev G, Akoya Biosciences).

Reagents were prepared and loaded into appropriate reservoirs on the instrument, and the prepared reporter plate was loaded into the instrument. A new PhenoCycler run was initiated using the experimental protocol design. A blank flow cell was loaded into the Flow Cell Slide Carrier, and all software prompts during the pre-flight routine were followed. The Sample Flow Cell was loaded into the carrier, and a leak check was performed. Automatic sample detection was performed, followed by scan region selection and imaging initiation. Upon completion, the Sample Flow Cell was placed in the Storage Buffer at 4°C. The generated QPTIFF data files were used for downstream image analysis. Analysis of the akoya multispectral immunofluorescence imaging was done as previously described.[68]

Please cite this article in press as: Sloan et al., A sex-specific platelet switch controls anti-tumor immunity in glioblastoma, Cancer Cell (2026), https://doi.org/10.1016/j.ccell.2026.10.004

PhenoCycler-fusion data analysis

We leveraged InstanSeg, an embedding-based deep learning model built for cell segmentation, to identify cell boundaries in each region of interest (ROI) extracted from the highly multiplexed immunofluorescence images generated by the Akoya PhenoCycler Fusion.[49] The resulting segmentation mask and a list of de-multiplexed single-channel images from the panel are input to Nimbus,[50] a deep learning model that predicts confidence of marker positivity in each cell. These scores, calculated for each channel and bounded between 0 and 1, replace integrated expression for downstream analyses to combat technical confounders like background staining, autofluorescence, and channel intensity variation.

By aggregating Nimbus scores across every high-quality ROI into a single AnnData object, we applied FlowSOM,[51] an unsupervised clustering algorithm based on self-organizing maps, to group cells by their pattern of protein expression. Using the markers enriched in each of the 18 resulting clusters, as identified by the Wilcoxon rank-sum test, we manually annotated cell states. We then appended these annotations to the spatial coordinates of each cell for further analysis.

To capture acellular features in each ROI, such as platelets, we employed a deep learning model for single-channel bright spot detection in fluorescence microscopy images called Spotiflow.[69] To efficiently calculate the density and proximity of these features around cells, we applied the cKDTree algorithm from the scipy.spatial library.[70] By aggregating these spatial association metrics for each previously defined cell state and comparing across ROI-specific metadata, we investigated sex-specific and treatment-correlated phenotypes.

QUANTIFICATION AND STATISTICAL ANALYSIS

Data visualization and statistical analysis were conducted using GraphPad Prism (Version 9, GraphPad Software Inc., RRID:SCR_002798). Depending on the dataset, unpaired or paired t-tests, as well as one-way or two-way analysis of variance (-ANOVA) with multiple comparison adjustments, were applied as described in the figure legends. Survival analysis was evaluated using the log rank test. For all analysis, statistical significance was set at $p < 0.05$.